

Generative Artificial Intelligence Navigated Development of Solvents for Next Generation High-Performance Magnesium Batteries

Xiang Gao, Ao-Qi Yang, Wen-Bei Yu, Jia-Cong Zhou, Mao-Jun Pei, Jia-Cheng Chen, Wei Yan, Guo-Qiang Luo, Yao Liu,* Jian-Hua Xiao,* and Jiujun Zhang*

Traditional trial-and-error methods are inefficient and costly in discovering novel solvents for next-generation magnesium (Mg) metal-based batteries. Therefore, this work establishes a simple yet efficient screening criterion for solvents by integrating artificial intelligence techniques with a virtual molecular database, potentially revolutionizing the traditional solvent design pathway. A total of 823 solvents are generated using a self-developed algorithm, and LUMO, Δ LUMO, ESP_{\min} , ESP_{\max} , and E_b are identified to establish the screening criterion through the analysis with machine learning (ML) models. Eighteen candidate solvents are successfully identified, and two of which are subsequently selected and experimentally validated, i.e., C1COCOC1 and COCC(C)OC (abbreviated as “DOX” and “DMP”). Notably, neither of these solvents has been previously reported for use in Mg batteries. Experimental results indicate that the DOX solvent, when paired with the Mg boron-based salt, i.e., $\text{Mg}[\text{B}(\text{hfip})_4]_2$, can significantly enhance the electrochemical performance. At a current density of 1.0 mAcm^{-2} , the average coulombic efficiency for Mg plating/stripping reaches 99.54 % after 5200 cycles. Furthermore, the Mg//Cu cell achieves a cumulative capacity exceeding 2000 mAhcm^{-2} , surpassing previously reported results. In summary, this work establishes a virtual molecular database and develops a streamlined screening methodology for Mg battery solvents based on their physicochemical properties, reducing the candidate pool from 823 to 18 and improving efficiency by nearly 50-fold. This research paradigm is not limited to the development of Mg batteries and can be readily extended to the exploration of other battery systems.

1. Introduction

Exploring clean and sustainable energy sources, such as solar, wind, and hydropower, has become essential for reducing dependence on fossil fuels, which are limited in supply and emit substantial pollutants.^[1–3] In this regard, the development of electrochemical energy storage and conversion technologies to manage the intermittent output of renewable energy sources has attracted significant attention. Among various electrochemical energy systems, batteries based on lithium (Li), sodium (Na), zinc (Zn), and magnesium (Mg) have been developed, with some already achieving commercial success.^[4–7] For instance, lithium-ion batteries (LIBs) have dominated markets in portable electronics and electric vehicles, owing to their high energy density and long cycle life.^[8,9] Nevertheless, the limited resource availability raises sustainability concerns, and the practical energy density and safety of LIBs remain inadequate to meet the demands of long-range travel and fully reliable operation.^[10] Consequently, the demand for next-generation rechargeable batteries has become increasingly urgent in light of current limitations.^[11–14]

At the current state-of-the-art, rechargeable Mg metal batteries (RMBs) are considered

as a promising alternative due to the high theoretical volumetric energy density of the anode,^[15] i.e., 3833 mAhcm^{-3} , and the abundance,^[16] which is over 1000 times greater than that of Li. Compared to LIBs, the relatively low reduction potential (-2.38 V vs. the standard hydrogen electrode) in RMBs promotes the formation of a passivation layer on the anode surface, which hinders the transport of Mg^{2+} .^[17] Hence, the rational design and optimization of Mg battery electrolytes offer a viable strategy to regulate interfacial reactions, thereby effectively addressing these challenges.^[18,19] Given that complete Mg battery electrolytes typically consist of Mg salts and primary solvents, electrolyte optimization encompasses two main strategies: the development of novel Mg salts and the design of advanced solvent systems. Previously reported Mg salts include $\text{Mg}(\text{pftb})_2$,

X. Gao, A.-Q. Yang, W.-B. Yu, J.-C. Zhou, M.-J. Pei, J.-C. Chen, W. Yan, Y. Liu, J.-H. Xiao, J. Zhang
 College of Materials Science and Engineering
 Fuzhou University
 Fuzhou, Fujian 350108, China
 E-mail: yao.liu@fzu.edu.cn; jhxiao@fzu.edu.cn; jiujun.zhang@fzu.edu.cn

G.-Q. Luo
 State Key Lab of Advanced Technology for Materials Synthesis and Processing
 Wuhan University of Technology
 Wuhan, Hubei 430100, China

 The ORCID identification number(s) for the author(s) of this article can be found under <https://doi.org/10.1002/adma.202510083>

DOI: 10.1002/adma.202510083

Mg(hfip)₂, MgCl₂, MgHMDS₂, MgTFSI₂, and MgOTf₂.^[20–25] More recently, novel Mg salts featuring boron-, aluminum-, and carborane-based cluster structures, e.g., Mg(B(hfip)₄)₂, Mg(Al(hfip)₄)₂, Mg(CB₁₁H₁₂)₂, have attracted considerable interest due to their excellent electrochemical performance in Mg batteries.^[11,26,27] Concerning practical solvents, tetrahydrofuran (THF), 1,2-dimethoxyethane (DME), diglyme (DG), tetruglyme (TG), amines (MOPA, MOEA), and imidazole-based cosolvents (MeIm, PrIm) serve as representative examples.^[11,24,28–31] It is evident that only a limited number of Mg salts and solvents (fewer than a dozen) have demonstrated practical utility over the past few decades, highlighting the difficulty in discovering novel materials. This limitation stems from the reliance on trial-and-error strategies, which can be more time-consuming and resource-intensive given the complexity of electrochemical reactions within battery systems. In the case of solvents, the virtually limitless chemical space, estimated at 10⁶⁰ possible organic molecular candidates, far exceeds the capacity of human intuition to explore effectively, rendering the development of novel Mg solvents particularly challenging.^[32,33] Therefore, leveraging advanced technologies, such as artificial intelligence (AI), to explore alternative research paradigms is essential and has attracted growing interest within the research community.

With the rapid advancement of AI technologies, including its subset machine learning (ML), these approaches have emerged as powerful tools in the field of battery research.^[34–38] Nevertheless, for an extended period, the widespread application of AI and ML has been mainly limited to predicting battery cycling performance or degradation. Although AI technologies hold great promise for accelerating the discovery of new materials and perhaps even catalyzing a new materials revolution, progress in this domain has thus far been relatively limited. It can be attributed to the fact that material performance is governed by multiple interdependent factors, leading to the absence of well-defined quantitative indicators. Limited data availability also hinders the understanding of mechanisms, thereby constraining the development of advanced materials. In recent years, the emergence of generative AI presents a promising solution to data scarcity, giving rise to a new research paradigm in materials development, i.e., the top-down material screening. Specifically, generative artificial intelligence is employed to construct a virtual molecular database, from which candidate materials are identified via high-throughput screening. This inverse design paradigm for materials discovery exhibits significant potential for uncovering previously unreported compounds. Recently, Wu et al. constructed a virtual library comprising millions of candidate organic semiconductors and developed a closed-loop screening workflow, thus enabling the efficient discovery of novel hole-transporting materials with tailored properties for solar cell application.^[39] Meanwhile, Jia et al. employed oxidative stability, synthetic accessibility, and solvation capability as screening criteria to identify promising fluoroether solvent candidates for high-voltage lithium metal batteries from a self-constructed virtual electrolyte library.^[40] Pan et al. employed an AI-assisted high-throughput screening strategy to identify two novel electrolyte additives (CA and HN) from a library of 75 000 molecules, which significantly enhanced the cycling stability and the performance of aqueous zinc-ion batteries.^[41] It is noteworthy that research integrating AI technologies to guide the discovery of

novel materials is presently undergoing rapid and exponential growth.^[42,43]

Inspired by these scenarios, the integration of large-scale virtual molecular libraries with well-defined screening criteria holds considerable promise for fundamentally accelerating the discovery of new solvents for Mg metal batteries. Nevertheless, two fundamental limitations, i.e., the availability of suitable virtual material databases and the establishment of robust screening criteria, need to be resolved before this research paradigm can be effectively applied to the exploration of Mg solvents.^[44–46] Concerning the construction of suitable virtual databases for Mg solvents, the difficulty primarily stems from the selective inclusion or exclusion of specific functional groups based on their electrochemical compatibility. For instance, functional groups such as acids, alcohols, and ketones have been recognized as unsuitable for Mg battery systems, based on empirical evidence from trial-and-error studies. Accordingly, molecules containing such groups should be excluded during the database construction process to avoid unproductive screening and minimize unnecessary computational effort. Nevertheless, databases with such requirements are either still under development or not yet publicly accessible, highlighting the urgent need to develop new algorithms in this field. In addition, no definitive screening criteria have yet been established for battery solvents, owing to the inherent complexity of electrochemical reactions. The effective identification of candidate solvents from large virtual databases remains challenging, and the performance of selected candidates is often suboptimal or unsuitable for practical application. It should also be acknowledged that with the advancement of computational chemistry, several descriptors have been introduced to partially evaluate the performance of candidate solvents. Based on the interaction between Li⁺ and solvent, He et al. recently identified the electrostatic potential (ESP) as a descriptor for solvent design.^[47] The ESP, which reflects the nuclear and electronic distributions within a molecule, provides valuable insights into molecular reactivity and captures the electronic response as molecules approach reactants.^[48–50] Therefore, the interaction between metal cations and electrolyte solvents can be effectively characterized through this descriptor. At the same time, Zhang et al. conducted a systematic investigation of the lowest unoccupied molecular orbital (LUMO) energy levels and other critical properties of organic solvents via various ML models.^[51] Their findings demonstrate that the LUMO energy level plays a critical role in determining the stability of coordinated ion-solvent complexes, analogous to the influence of ESP. Although ESP and LUMO provide a valuable framework for interpreting the solvation structure in battery systems and serve as critical descriptors for evaluating the solvent suitability, it is important to acknowledge that they remain insufficient for the efficient discovery of practical solvents due to the absence of well-defined screening thresholds. As a result, the development of simple yet effective screening criteria capable of reliably identifying suitable solvents for Mg metal batteries from large virtual molecular databases remains a significant challenge, particularly in the context of real-world applications.

In response to the above challenges, this study proposed a simple yet effective method for successfully screening high-performance solvents for Mg metal batteries from a virtual molecular database. By employing a self-developed matrix engineering algorithm, a diverse array of organic molecules was

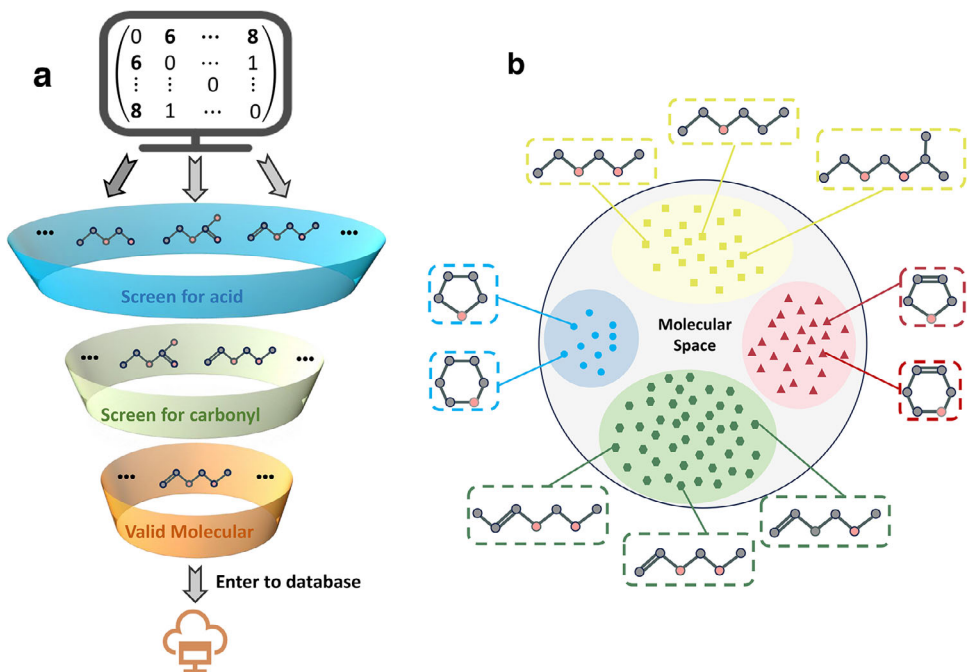


Figure 1. a) Schematic of the matrix engineering generation algorithm. b) Visualization and classification of the solvent molecular database. The chain with double bonds ($C=C$), chain with single bonds ($C-C$), ring with double bonds ($C=C$), and ring with single bonds ($C-C$) are marked in green, yellow, red, and blue, respectively.

rapidly generated, and unsuitable functional groups were effectively excluded, such as acids, alcohols, and carbonyl, thereby improving compatibility with Mg battery systems. As a result, a database comprising 823 virtual solvent molecules was constructed for screening, with each containing up to eight main atoms, e.g., C and O. The physicochemical properties of molecules were systematically explored, revealing a strong correlation with the presence of $C = C$ and $C - C$ bonds, while exhibiting minimal dependence on the linear or cyclic nature of the molecular structure. Based on the average MAE results across 13 different ML models, LUMO, Δ LUMO, ESP_{min} , ESP_{max} , and E_b were selected to establish the screening criterion. As expected, 18 target molecules were identified, narrowing the pool from 823 candidates and improving efficiency nearly 50-fold. Thereafter, two promising molecules were selected for further experimental investigation, i.e., 1,3-Dioxane (C1COCOC1, abbreviated as "DOX") and 1,2-Dimethoxypropane (COCC(C)OC, abbreviated as "DMP"). At a current density of 1.0 mAcm^{-2} , the Mg//Cu cell containing DOX achieved an average coulombic efficiency of 99.54 % for Mg plating/stripping over 5200 cycles. Compared with DME, the cycle life was extended by nearly an order of magnitude, with a cumulative capacity exceeding 2000 mAcm^{-2} , surpassing previously reported results. To further validate the feasibility of this approach, three solvents previously identified as unsuitable for Mg batteries through earlier trial-and-error studies were re-examined. Both computational analysis and battery cycling experiments demonstrated that solvents whose physicochemical properties fail to meet the established screening criterion rapidly induce battery failure, thereby confirming the validity of this research paradigm from a reverse perspective. The database was further employed to screen solvents for Na and K

metal batteries, further demonstrating the broader applicability of this approach. All in all, the integration of a self-constructed virtual database with the proposed screening criterion fundamentally transforms the processes of discovery and development, significantly enhancing the efficiency of novel Mg solvent exploration. Notably, this approach is conceived not merely as a theoretical framework but as a practical tool for identifying viable solvents. Furthermore, its applicability extends beyond Mg metal batteries and can be adapted to the exploration of other energy storage systems.

2. Results and Discussion

2.1. Physicochemical Properties of the Molecules

Figure 1a and Figure S1 (Supporting Information) present schematic diagrams illustrating the one-to-one mapping between matrix elements and molecules, along with the overall logical framework of this study. The quality and compatibility of the virtual database are critical for the effective screening and identification of target solvents. Detailed descriptions of the pre-processing procedures employed in database construction are provided in the Supporting Information. Solvents containing the carbonyl group ($C = O$) have been widely utilized in other battery systems,^[2,52] while empirical evidence indicates that such molecules are unsuitable for Mg batteries. It remains an open question whether the presence of a double bond inherently renders all molecular solvents incompatible for Mg batteries, or if this limitation is specific to the carbonyl group. To partially address this issue, molecules containing carbon-carbon double ($C = C$) bonds are also included in the virtual database. Acids and

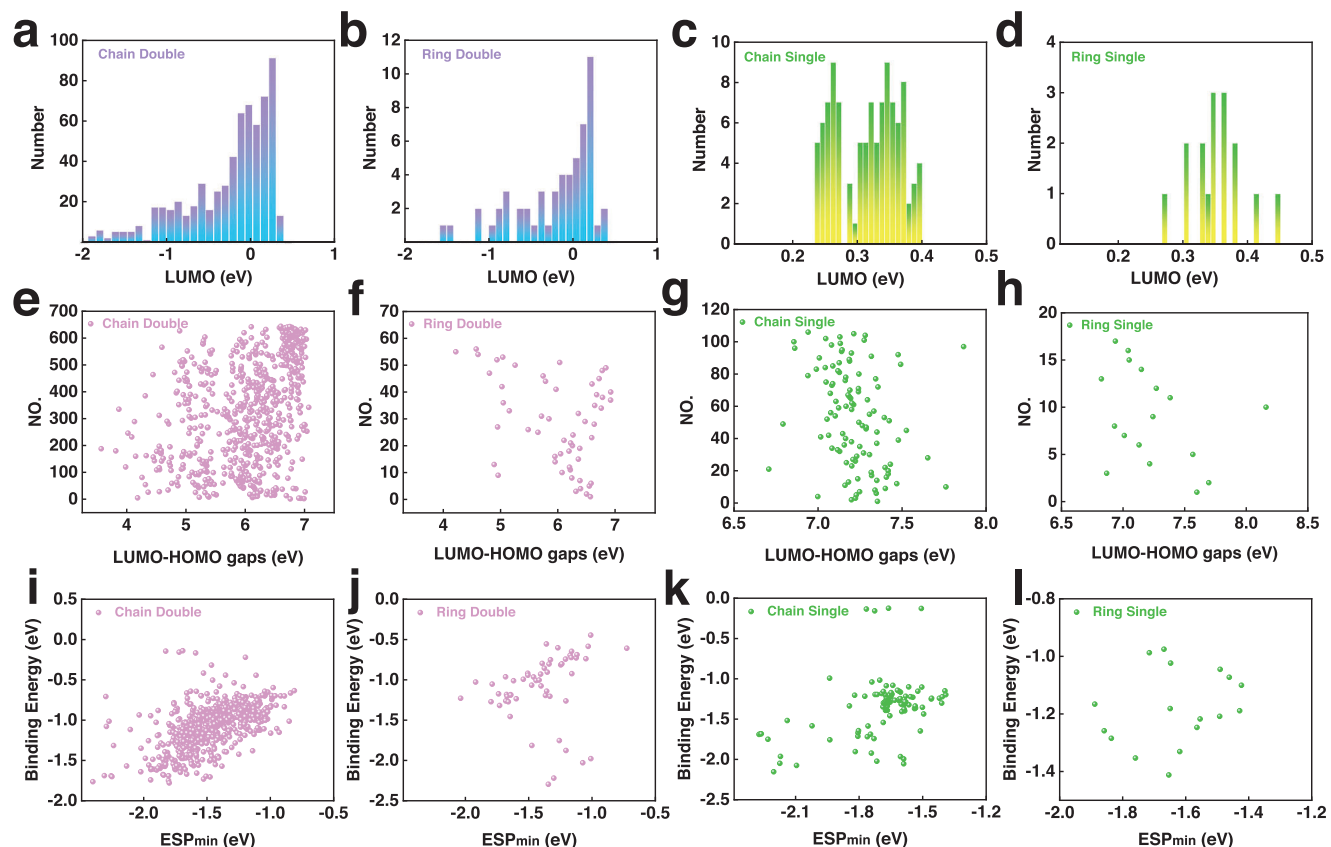


Figure 2. a-d) Distribution of LUMO energy levels for constructed molecules featuring chain with double bonds, chain with single bonds, ring with double bonds, and ring with single bonds. e-h) The corresponding energy gap ($E_g = \text{LUMO} - \text{HOMO}$) distribution. i-l) The relationship between ESP_{\min} and the binding energy of Mg (E_b).

alcohols are excluded from consideration,^[20,53] and this filtering procedure ensures the resulting molecules are theoretically suitable for investigation, rather than randomly generated with limited practical applicability. As a result, the self-constructed virtual database comprises a total of 823 solvent molecules, each containing up to eight main atoms, e.g., C and O, with the detailed SMILES provided in File S1 (Supporting Information).

As illustrated in Figure 1b, all 823 molecules are classified into four categories, e.g., chain with double bonds (C = C), chain with single bonds (C – C), ring with double bonds (C = C), and ring with single bonds (C – C), with corresponding counts of 644, 106, 56, and 17, respectively. It should be acknowledged that this distributional discrepancy may hinder the performance of subsequent ML models, particularly in the small-sample scenario. Nevertheless, in this study, the high-throughput screening of virtual molecules has been conducted based on their calculated physicochemical properties rather than predicted values. Consequently, the molecular distribution may influence the performance of ML models, but the screening outcomes are not adversely affected. Notably, Figure 1b serves as an illustrative representation of molecules with different topologies, rather than as an actual visualization of the database. Quantum chemical calculations are subsequently conducted, and the following physicochemical properties are summarized to gain new insights into pure solvents, e.g., LUMO, HOMO, E_g , ESP_{\max} , ESP_{\min} .^[18,19,47,51,54,55]

Additionally, ion-solvent interactions have recently attracted considerable attention in discussions of the solvation structure. The binding energy (E_b) of the Mg²⁺-solvent complex and the change in LUMO energy levels ($\Delta\text{LUMO} = \text{LUMO}_{\text{Mg}} - \text{LUMO}$) upon coordination are also investigated. Here, the statistical data for LUMO, E_g , and ESP_{\min} are selected as representative examples for discussions and are illustrated in Figure 2, while additional results are presented in Supplementary Figure S10 to S13.

It can be observed that the physicochemical properties of molecules are primarily governed by the presence of C – C and C = C bonds, with minimal impact of structural features, such as linear or cyclic configurations. Figure 2a-d illustrates that molecules containing C = C bonds exhibit the relatively lower LUMO energy levels compared to those with C – C bonds, with values ranging from -2.0–0.5 eV vs. 0.2–0.5 eV. As shown in Figure S15 (Supporting Information), the LUMO energy levels range from -3.5 to -2.5 eV for Mg²⁺-solvent complexes, compared to -2.0–0.5 eV for corresponding pure solvents containing C = C bonds. Regarding molecules with C – C bonds, the LUMO energy levels range from -3.5 to 2.5 eV for complexes, versus 0.2 to 0.4 eV for the solvents. It indicates that molecules coordinated with Mg²⁺ generally result in a reduction of the LUMO energy levels, regardless of containing C = C or C – C bonds, thereby decreasing the reductive stability, which is consistent with previous studies.^[56,57] Figure 2e-h illustrates that the

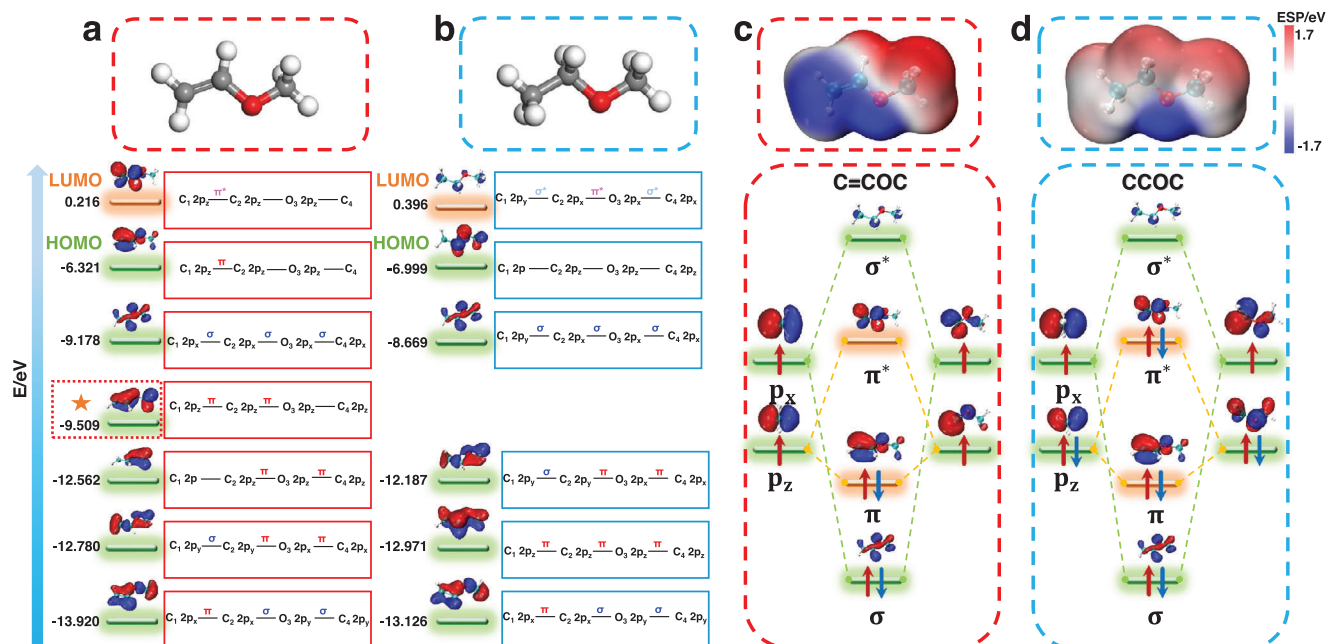


Figure 3. a,b) The molecular orbitals of $\text{C}=\text{C}-\text{O}-\text{C}$ and $\text{C}-\text{C}-\text{O}-\text{C}$, respectively, c,d) and the corresponding energy level splitting diagrams.

E_g values of molecules containing $\text{C}=\text{C}$ bonds are generally distributed within the range of 4.0–7.0 eV, whereas those with $\text{C}-\text{C}$ bonds fall within the narrower range of 7.0–7.5 eV. It is well established that a smaller E_g facilitates electron transitions from the HOMO to the LUMO energy level, thereby enhancing electronic transport. Nevertheless, solvents with reduced E_g not only narrow the electrochemical window but also compromise the thermal stability of the resulting electrolytes, rendering them more susceptible to decomposition at elevated temperatures, which can adversely impact the lifespan of Mg batteries. Figure S11 (Supporting Information) illustrates the binding energies of Mg^{2+} -solvent complexes, revealing comparable values for both chain and ring configurations. More specifically, the binding energies of molecules containing $\text{C}=\text{C}$ bonds range from -1.5 to -0.5 eV, with most values concentrated \approx -1.0 eV, whereas those with $\text{C}-\text{C}$ bonds range from -2.0 to -1.0 eV, with a median value of \approx -1.2 eV. Figure 2i to 2l depict the relationship between E_b and ESP_{\min} , demonstrating that the lower ESP_{\min} values correspond to the higher E_b , thereby facilitating electron transfer from the solvent to Mg^{2+} . These findings are further supported by Figure S18 (Supporting Information), which illustrates that the increased electron transfer leads to a reduction in bond length, thereby enhancing E_b . As shown in Figure S17 (Supporting Information), Mg^{2+} preferentially coordinates with the oxygen atoms of molecules during the complex formation. Regions of higher electron density on the molecular surface are more prone to form strong coordination bonds with positively charged ions. Nevertheless, molecules characterized by excessively high electronegativity should also be avoided in screening candidate solvents, as they may hinder the desolvation of Mg^{2+} -solvent complexes. Figure S10 (Supporting Information) presents the ΔLUMO values to provide more insight into the solvation structure, showing that molecules containing both $\text{C}=\text{C}$ and $\text{C}-\text{C}$ bonds have comparable values falling in the range of -3.5 to -2.5 eV. Figures S12

and S13 (Supporting Information) illustrate the distributions of ESP_{\max} and HOMO, respectively, further revealing the trend that the physicochemical properties are governed by the presence of double or single bonds. Additionally, similar to the LUMO results, the HOMO energy levels of all solvent molecules decreased upon coordination, indicating enhanced oxidative stability,^[58] as depicted in Figure S19 (Supporting Information).

To further elucidate the differences in physicochemical properties between $\text{C}=\text{C}$ and $\text{C}-\text{C}$ bonds, $\text{CH}_2\text{CHOCH}_3$ and $\text{CH}_3\text{CH}_2\text{OCH}_3$ (abbreviated as $\text{C}=\text{C}-\text{O}-\text{C}$ and $\text{C}-\text{C}-\text{O}-\text{C}$) are selected as benchmark molecules for detailed investigation from a molecular orbital perspective. The LUMO energy level of $\text{C}=\text{C}-\text{O}-\text{C}$ is lower than that of $\text{C}-\text{C}-\text{O}-\text{C}$ due to the presence of a $\text{C}=\text{C}$ bond, with values of 0.216 and 0.396 eV, respectively. The ESP_{\min} (ESP_{\max}) values of these two molecules are -1.365 (1.087) and -1.645 eV (0.566 eV). To minimize potential misunderstandings and simplify the description, atoms are labeled as $\text{C}_1\text{C}_2\text{O}_3\text{C}_4$ in the subsequent context. As shown in Figure 3a,b, most molecular orbitals of these two molecules are comparable; therefore, they are omitted from the discussion. Two representative orbitals are highlighted to show the similarity, with the energy levels of -13.920 ($\pi-\sigma-\pi$) and -9.178 eV ($\sigma-\sigma-\sigma$) in $\text{C}_1=\text{C}_2-\text{O}_3-\text{C}_4$, and the corresponding levels of -13.126 and -8.669 eV in $\text{C}_1-\text{C}_2-\text{O}_3-\text{C}_4$. Moreover, the orbital at an energy of -12.780 eV in $\text{C}_1=\text{C}_2-\text{O}_3-\text{C}_4$ can also be compared to the corresponding energy level of -12.187 eV in $\text{C}_1-\text{C}_2-\text{O}_3-\text{C}_4$, with both exhibiting a $\sigma-\pi-\pi$ configuration. In contrast, the $\pi-\pi-\pi$ configuration can only be observed in $\text{C}_1-\text{C}_2-\text{O}_3-\text{C}_4$ at an energy level of -12.971 eV, whereas $\text{C}_1=\text{C}_2-\text{O}_3-\text{C}_4$ exhibits $\pi-\pi$ configurations between the $\text{C}_1=\text{C}_2-\text{O}_3$ and $\text{C}_2-\text{O}_3-\text{C}_4$ segments, with corresponding energy levels of -9.509 and -12.562 eV, respectively. For the molecular orbital with an energy level of -12.562 eV, the π bond between C_2-O_3 can further interact with the p orbital of either C_1 or C_4 in

$C_1 = C_2 O_3 C_4$, resulting in $p - \pi$ conjugation. Consequently, the distinction between these two molecules is determined by the $\pi - \pi$ and $\pi - \pi - \pi$ configurations, which modulate the electronic structure and result in a lower LUMO level in $CH_2 CHOCH_3$ containing a $C = C$ bond. Figure 3c,d further highlights the distinction in physicochemical properties through bond order analysis. For the purpose of discussion, the molecules $CH_2 CHOCH_3$ and $CH_3 CH_2 OCH_3$ are partitioned into CH_2 and $CHOCH_3$, and CH_3 and $CH_2 OCH_3$, respectively. $CH_3 CH_2 OCH_3$ contains two more proton than $CH_2 CHOCH_3$, and this difference in electron count results in full occupation of the π^* bond. Consequently, the LUMO energy level of $CH_2 CHOCH_3$ is predominantly determined by the π^* bond, whereas that of $CH_3 CH_2 OCH_3$ exhibits σ^* bond characteristics. These findings support the analysis presented in Figure 3a,b, demonstrating that the lower LUMO energy levels of generated molecules are primarily attributed to the presence of $C = C$ bonds. A similar analysis, along with corresponding results for ring structures, i.e., $C_1 = COCO_1$ and $C_1 - COCO_1$, as presented in Figure S16 (Supporting Information).

All in all, these findings provide new insights into the widespread use of single-bond molecules as battery solvents, as their enhanced stability reduces the likelihood of undesirable side reactions. In contrast, molecules containing double bonds have relatively low LUMO energy levels and are more receptive to electrons.^[18] Although this characteristic can be advantageous in certain scenarios, the lower LUMO energy levels also increase the risk of spontaneous reactions with the electrodes. In the case of Mg batteries, the formation of a passivation layer may be facilitated by solvents with lower LUMO energy levels, thereby partially addressing the question of whether the presence of a double bond inherently renders molecular solvents unsuitable.

2.2. Machine Learning

As described in Section 2.1, the physicochemical properties of solvents are closely related to their molecular characteristics, such as the presence of $C - C$ and $C = C$ bonds. Although the preceding discussion emphasizes the distinctions in LUMO energy levels among various molecules from an electronic perspective and provides related explanations, evaluating the suitability of solvents for Mg metal batteries based solely on a single criterion remains inadequate. Therefore, elucidating the high-dimensional correlations between physicochemical properties and molecular characteristics is essential for developing more comprehensive and effective screening criteria. To this end, 13 different ML models are employed and the detailed settings are summarized in Table S2 (Supporting Information). The performance of ML models is evaluated based on R^2 and MAE, calculated with Equations (5) and (6). Figure 4a presents the average MAE values of the physicochemical properties predicted by all ML models, assessed using both the training and test datasets. In addition to MAE, the relative error metric MAPE for all ML models has also been investigated, and the corresponding results are illustrated in Figures S7 and S8 (Supporting Information). The MAPE for HOMO remains below 6 % across all models, whereas for LUMO, it exceeds 200 % due to its near-zero values in many samples. This extreme variability underscores the unreliability of MAPE, particularly under small-sample con-

ditions; therefore, only MAE is discussed in the main analysis. It can be seen that E_g and HOMO exhibit the relatively high MAE values of 0.276 (0.378) and 0.235 eV (0.284 eV), respectively, and are therefore excluded from subsequent analysis. In contrast, LUMO, Δ LUMO, ESP_{max} , ESP_{min} , and E_b demonstrate the superior predictive performance and are selected for further investigation and the establishment of screening criterion. In Mg metal battery systems, the anode potential of -2.37 V renders reductive decomposition, rather than oxidative degradation at high voltages, the primary challenge.^[59] Consequently, HOMO-related oxidative stability is of limited relevance and may be reasonably excluded, further validating the aforementioned selection. Additionally, a five-fold cross-validation has been performed on the training set to validate the reliability of selected physicochemical properties, with the average MAE across folds presented in Tables S3–S9 (Supporting Information). The performance of models with cross-validation is comparable to that without it, and with slight degradation in some cases. This observation is primarily attributed to the limited sample size of the dataset and the inherent heterogeneity in the molecular distribution. Figure S9 (Supporting Information) demonstrates that the results obtained with and without cross-validation are consistent with the overall data trends, indicating that cross-validation primarily affects model accuracy without altering the selection of physicochemical properties.

Figure 4b and Figure S25 (Supporting Information) present the MAE and R^2 values of ESP_{min} , respectively. Among these models, the Bagging algorithm exhibits the lowest MAE and the highest R^2 on the training set, i.e., 0.057 eV and 0.916. Nevertheless, the GBR model demonstrates a smaller MAE compared to the Bagging algorithm on the test set, i.e., 0.151 eV, and has therefore been selected for further study. To improve the training efficiency and minimize the prediction bias, two critical hyperparameters are optimized using a grid search algorithm, e.g., the number of estimators and the learning rate. Figure 4c illustrates that the numbers of estimators are set to 50, 100, 150, 200, 250, and 300, while the learning rates are adjusted to 0.01, 0.05, 0.1, 0.2, 0.25, and 0.3. Under the circumstance, i.e., 300 estimators and a learning rate of 0.01, the GBR model achieves the optimal performance, with a negative mean error of -0.04 . Consequently, accurate ML models capable of predicting the physicochemical properties of molecules have been developed, thereby reducing the reliance on high-throughput calculations for large virtual databases in upcoming research. As illustrated in Figure 4d, the Pearson correlation coefficients are calculated based on the GBR model to gain new insights into the relationships among various features. Therefore, the complex, high-dimensional correlations between physicochemical properties and molecular characteristics are specifically investigated. For instance, the value between NumA and NumH is $p = 0.97$, indicating a strong relationship, whereas NumO and rCO exhibit a negative correlation as $p = -0.91$. Figure 4e presents the distribution of feature importance, revealing that the most influential factors affecting ESP_{min} are μ , AvgI, and R, with respective contribution rates of 40.7 %, 28.6 %, and 19.4 %. The cumulative feature importance exceeds 80 %, suggesting that concentrating on these features can effectively facilitate the regulation of ESP_{min} . Figure 4f displays that the calculated ESP_{min} values closely align with the prediction line generated by the GBR model. Specifically, the R^2 values for the

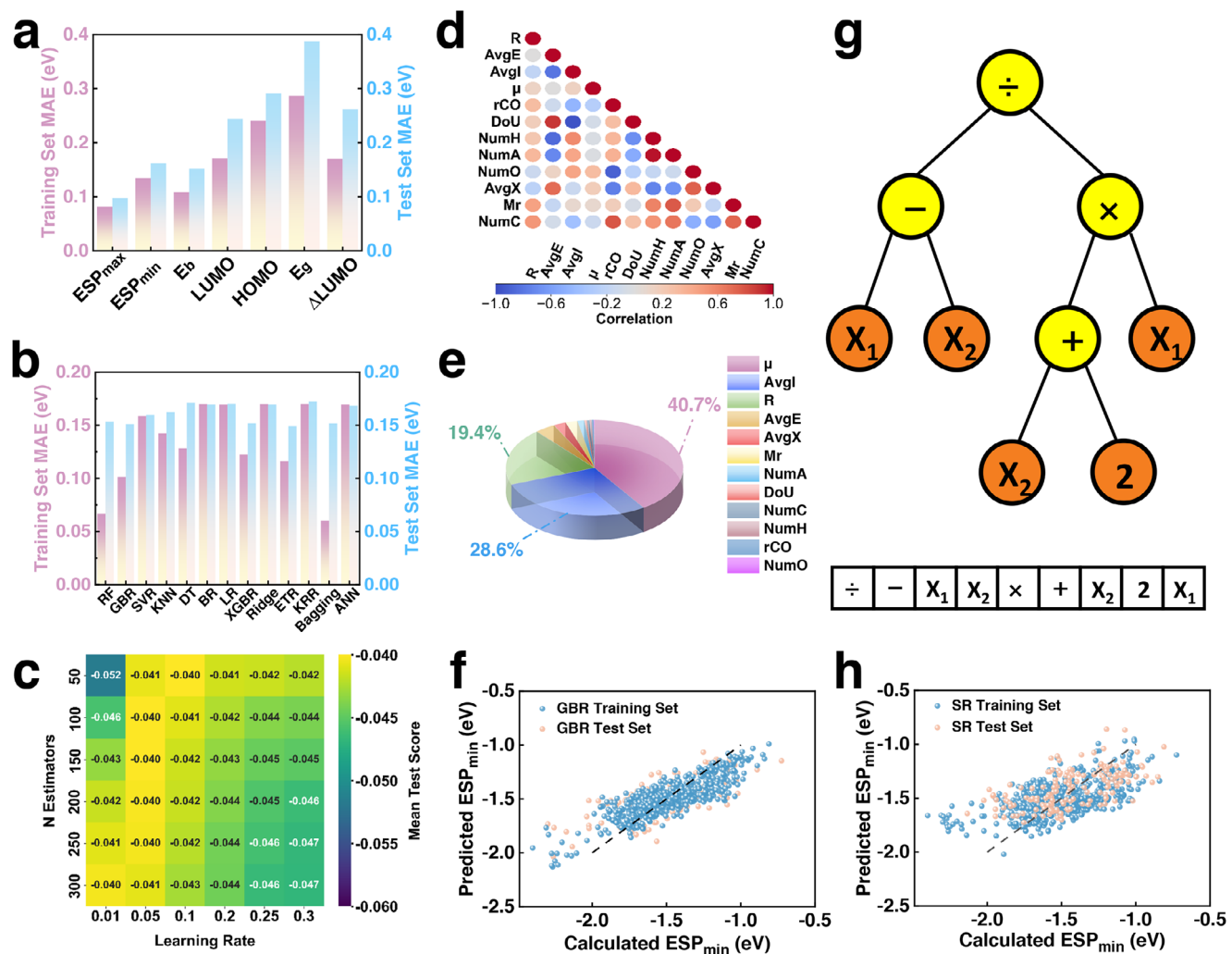


Figure 4. a) The average MAE of physicochemical properties for the training and test sets, respectively. b) The MAE of ESP_{\min} as calculated by various ML models. c) Diagram of the grid search algorithm for the GBR model. d) Pearson correlation coefficient plot of 12 features. e) Feature importance along with the corresponding proportions for the GBR model, with ESP_{\min} as the target value. f) Quantum chemical calculated ESP_{\min} versus the GBR model predicted values. g) Schematic of the symbolic regression (SR) algorithm. h) Calculated ESP_{\min} versus predicted values using the SR model.

training and test sets are 0.804 and 0.501, respectively, with corresponding MAE values of 0.088 and 0.151 eV. It should be acknowledged that this discrepancy indicates a certain degree of overfitting in the GBR model. Nevertheless, the primary objective of this study is to leverage ML models to elucidate the correlations between physicochemical properties and molecular characteristics, thereby enabling the establishment of effective screening criteria rather than serving solely as predictive tools. As shown in Figure S14 (Supporting Information), the critical features contributing to ESP_{\min} are illustrated. It can be seen that AvgI, μ , R, AvgE, and Mr exhibit consistent distributions between the training and test sets, further supporting the informative value of these features despite the moderate prediction accuracy under limited data conditions. Therefore, although overfitting may affect prediction accuracy, it does not compromise the validity of the screening results.

To further enhance the understanding of these correlations, a general descriptor for predicting ESP_{\min} has been proposed

using symbolic regression (SR) algorithms,^[60–62] providing improved interpretability. Based on the feature importance ranking shown in Figure 4e, μ and AvgI are selected as input parameters for constructing the descriptor, as expressed in Equation S1 (Supporting Information). In cases where molecules exhibit comparable μ values, a large AvgI leads to a more negative ESP_{\min} , thereby increasing E_b . Four representative molecules are selected as shown in Figure S26 (Supporting Information) to verify this hypothesis, with the dipole moments (μ) of 2.387, 2.381, 2.381, and 2.388, and the AvgI values of 12.724, 12.774, 12.821, and 12.913, respectively. The calculated and predicted ESP_{\min} values are -1.240 (-1.548), -1.614 (-1.608), -1.660 (-1.664), and -1.945 eV (-1.775 eV), validating the accuracy and reliability of the descriptor. Figure 4h presents a scatter plot of ESP_{\min} predicted by the SR model against the calculated values, demonstrating excellent overall predictive performance. Therefore, these findings demonstrate that the proposed descriptor offers a novel tool and perspective for understanding the electrostatic potential.

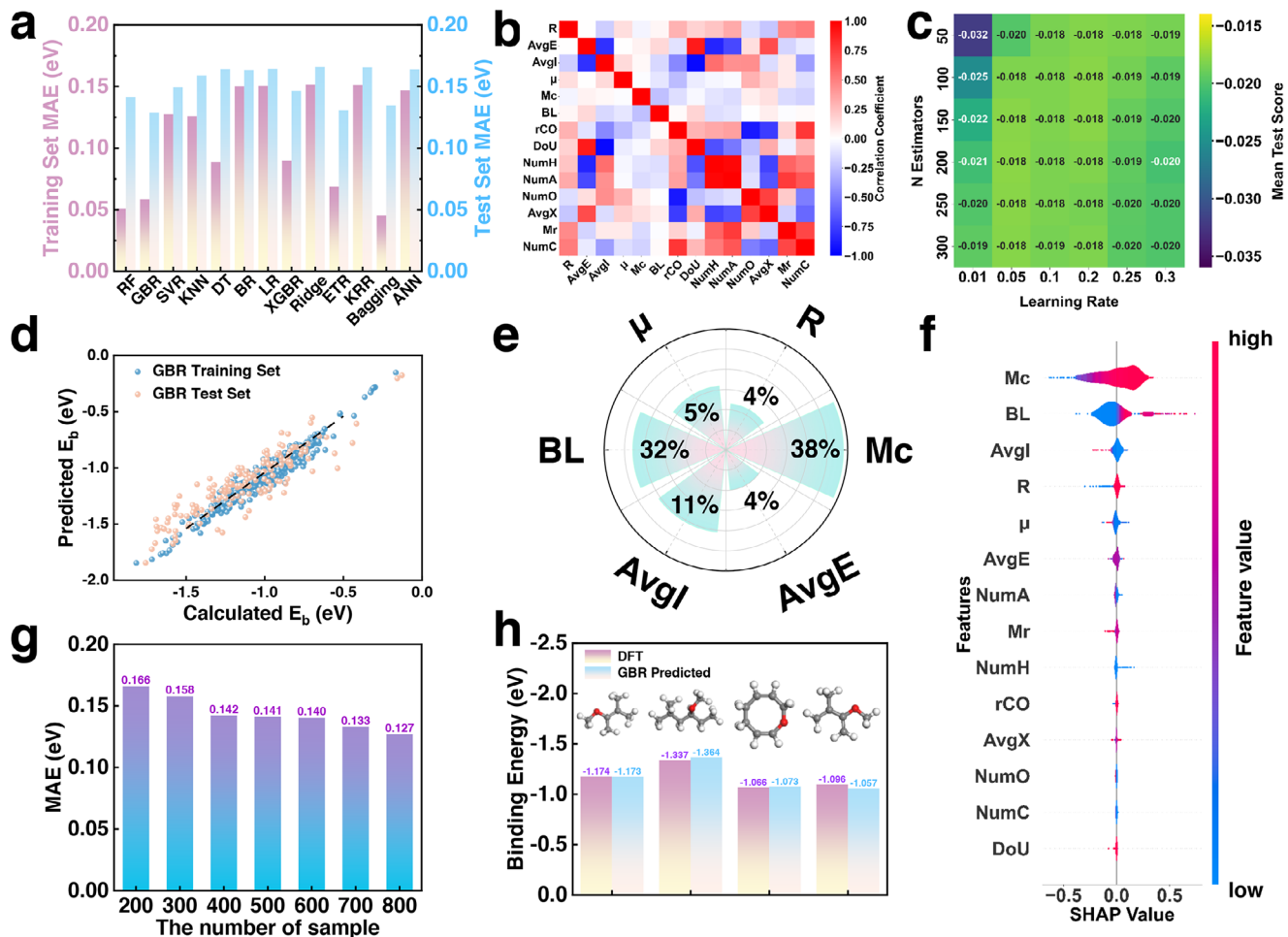


Figure 5. a) The MAE of E_b as calculated by various ML models, with training and test sets represented in purple and blue, respectively. b) Thermodynamic correlation coefficient plot for the GBR model. c) Diagram of the grid search algorithm for the GBR model. d) Scatter plot of actual vs. predicted values for binding energy. e) Radar chart of feature importance for the GBR model. f) SHAP plot of feature importance for the GBR model. g) Histogram depicting the distribution of model MAE values as a function of sample size. h) The predicted and calculated binding energies of selected molecules.

Ion-solvent complexes predominantly govern the solvation effect; therefore, E_b of Mg^{2+} -molecule interactions has also been investigated with various ML models. Figure 5a compares the MAE values of E_b for both the training and test sets. Consistent with the previous discussion, the GBR model has been selected, achieving the MAE of 0.129 eV. As shown in Figure 5c, the parameters optimization has been conducted using the grid search algorithm, resulting in optimal parameters identified as a learning rate of 0.05 and a maximum of 100 estimators. Figure 5b is the heat map of feature correlations, with AvgE and DoU showing a strong positive correlation, while rCO and NumO exhibiting a negative correlation, i.e., 0.89 and -0.91. Figure 5d illustrates the excellent accuracy of the GBR model, which has been subsequently applied to predict E_b in comparison with the calculated values. As shown in Figure 5h, these molecules are randomly selected from the database, and the calculated and predicted E_b are -1.174 (-1.173), -1.337 (-1.364), -1.066 (-1.073), and -1.096 eV (-1.057 eV), respectively. The maximum difference between these values is 0.04 eV, indicating that the binding energy of Mg^{2+} -solvent can be accurately estimated using

the GBR model. Figure 5g presents the MSE of E_b as a function of dataset size, e.g., 200, 300, 400, 500, 600, 700, and 800. As the dataset size increases to 800, the curve flattens and the error converges, i.e., from 0.166 to 0.127, confirming the reliability and robustness of the GBR model. Figure 5e highlights the most informative features for predicting E_b , with their respective importance as follows: 38 % (Mc), 32 % (BL), 11 % (AvgI), 5 % (μ), 4 % (R), and 4 % (AvgE). Here, Mc denotes the Mulliken charge of Mg^{2+} in the solvent complex, and BL represents the average Mg – O bond length, serving as an indicator of interaction strength. Additional properties are described in the corresponding section. The cumulative feature importance exceeds 94 %, and detailed information on the importance of all features is provided in Figure S27 (Supporting Information). It can be seen that Mc and BL play a significant role in E_b , consistent with previous findings, as stronger bonding facilitates electron transfer and leads to reduced bond lengths. As shown in Figure 5f, the SHAP analysis is also employed to enhance the model interpretability and to evaluate the contribution of each molecular feature to E_b . The feature importance rankings shown in Figure 5e,f are

largely consistent, thereby validating the results. The slight differences observed in the importance of R and μ may be attributed to the distinct ways in which the two methods account for feature interactions and non-linear effects. The remaining physicochemical properties, including ΔLUMO , ESP_{\max} , HOMO, LUMO, and E_b , are investigated and presented in Figures S20–S24 (Supporting Information), with the Bagging algorithm selected for further in-depth analysis. Despite variations in optimal estimators, learning rates, and feature importance across these properties, the model consistently exhibits excellent overall predictive performance.

2.3. Electrolyte Screening

As previously mentioned, discovering compatible solvents through traditional trial-and-error methods remains challenging and resource-intensive. Although the physicochemical properties of solvents significantly influence the performance of Mg metal batteries, the critical factor and the degree of interdependence among these properties have not yet been fully elucidated. Therefore, ML techniques are employed in Section 2.2 to systematically investigate the physicochemical properties of molecules and identify the decisive features. Building upon previous research findings, this section introduces a straightforward and effective methodology to screen potential organic solvents suitable for Mg metal batteries, utilizing the constructed virtual database. Figure S34 (Supporting Information) illustrates the underlying logic and rationale of this screening approach, which is grounded in the well-established materials science tetrahedron framework. This conceptual model emphasizes that materials with similar structures and properties generally demonstrate comparable performance. The generated molecules predominantly consist of carbon, oxygen, and hydrogen atoms, and exhibit similar topological features, including single and double bonds, as well as ring and chain configurations. When the physicochemical properties of the screened molecules closely align with those of solvents reported in the literature, it is reasonable to infer that these candidates hold considerable potential for successful application in Mg metal batteries. Therefore, the screening criterion is based on the principle that candidate molecules should exhibit physicochemical properties comparable to those of solvents that have been previously reported or are currently in practical use,^[63–65] e.g., 1,2-dimethoxyethane (DME), tetrahydrofuran (THF), diglyme (DG), tetraglyme (TG), and dioxolane (DOL).

As shown in Figure 4a, the physicochemical properties such as LUMO, ΔLUMO , ESP_{\min} , ESP_{\max} , and E_b exhibit higher predictive accuracy across the ML models and are therefore selected as the primary screening criteria. ESP_{\min} can reflect the coordination ability of a molecule toward cations, and ESP_{\max} provides insight into charge separation.^[47] During battery cycling, the solid electrolyte interphase (SEI) layer and associated side reactions are critical factors influencing battery performance and safety, both of which are closely associated with the LUMO energy level of the electrolyte.^[66] As demonstrated in Section 2.1, a decrease in the LUMO energy level upon cation coordination raises the reduction potential of the solvent, thereby increasing the likelihood of side reactions.^[51] Consequently, SEI formation can be partially inferred by evaluating the LUMO energy level, and the change

in LUMO before and after cation coordination (ΔLUMO) also significantly impacts battery performance. Additionally, E_b is a widely discussed indicator for evaluating the ability of solvents or anions to participate in the solvation shell of metal ions.^[67,68] It can be concluded that the overall framework of this approach is well-founded, with several practical influencing factors thoughtfully considered. Thus, this data-driven approach provides a scientifically grounded basis for the development of robust and effective screening criterion.

As outlined in Figure 6a, the physicochemical properties of widely reported or practically used solvents are defined as the acceptable range for the screening process. Notably, these values are obtained from quantum mechanical calculations performed on five benchmark solvents, employing computational parameters identical to those used for the molecular database. Compared to the interval shown in Figure 6a, the upper and lower limits have been expanded by ± 0.01 eV to increase the number of potentially usable solvents.^[69,70] For each physicochemical property, the defined range establishes a threshold window under the assumption that novel solvents falling within these limits will exhibit comparable performance. All 823 solvents are subsequently screened with the self-defined threshold, as demonstrated in Figure 6b. It relies on data similarity to identify potential molecules, resulting in the screening of only 18 feasible solvents for Mg batteries from the virtual database, and the corresponding physicochemical properties are shown in Table S10 (Supporting Information). Here, Figure 6c illustrates only a subset of the screened molecules, demonstrating that most of the candidate solvents lack C = C bonds. This phenomenon attributes the fact that C = C bonds tend to lower the LUMO energy level, making the corresponding solvents more susceptible to electron acceptance during electrochemical reactions, which can trigger side reactions that degrade battery performance and reduce lifespan. In addition, carbonyl-containing solvents have been deemed unsuitable for Mg battery systems.^[71,72] To further validate this screening methodology, the self-developed algorithm generates an additional database including 413 carbonyl-containing organic solvents, with detailed SMILES provided in Supporting File 3. As shown in Figure S28 (Supporting Information), the LUMO energy levels of these solvents fall significantly below the defined screening threshold and are therefore excluded based on the proposed criteria, i.e., 0.238–0.389 eV.

To ensure the screening criteria more transparent and reproducible, Figures S29–S33 (Supporting Information) present the plots of LUMO, ESP_{\min} , ESP_{\max} , E_b , and ΔLUMO for the 18 screened molecules compared with the 823 molecules in the original dataset. Tables S11–S15 (Supporting Information) provide the detailed percentile positions of these molecules for each property, with the percentile statistics arranged from the lowest to the highest values. It can be observed that the LUMO energy levels are highly concentrated within the 90–100% range, which in turn results in ΔLUMO values being similarly clustered, at ≈ -3.4 to -3.5 eV. Nevertheless, the ranges of ESP_{\min} and ESP_{\max} are relatively dispersed, suggesting that the selection criteria for certain crucial physicochemical properties lack consistency, thereby underscoring the challenges associated with identifying new solvents through conventional trial-and-error methods. In conclusion, these findings may partially address the previously raised question of whether the presence of a double bond

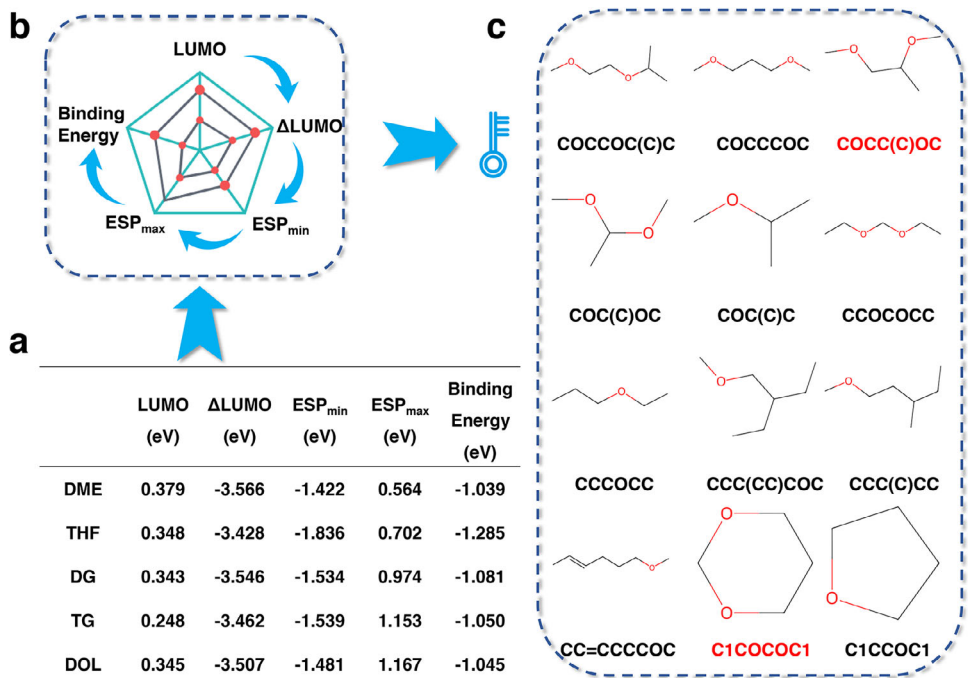


Figure 6. a) The calculated physicochemical properties of practical electrolytes. b) Schematic of the screening criterion, and c) the target molecules screened from the 823-entry database.

inherently renders all molecular solvents unsuitable for use in Mg batteries. Furthermore, they reinforce experimental observations that carbonyl-containing molecules are unsuitable for Mg battery applications and validate the effectiveness of the proposed screening criteria from an experimental standpoint. Compared to the traditional trial-and-error paradigm, this screening approach reduces the pool of candidate solvents from 823 to 18, improving screening efficiency by nearly 50-fold. Moreover, the majority of these candidate molecules have not been previously reported, highlighting the potential of this research paradigm for discovering novel solvents.

2.4. Experimental Verification

To validate the effectiveness of these candidate solvents in practical, 1,2-Dimethoxypropane (COCC(C)OC, abbreviated as DMP) and 1,3-Dioxane (C1COCOC1, abbreviated as DOX) were selected for experimental verification of their compatibility with the Mg anode, based on toxicity and availability. Mg[B(hfip)₄]₂ was selected as the Mg salt to prepare the corresponding electrolytes using DOX, the conventional ether-based solvent DME, and their mixture, respectively. The obtained electrolytes are referred to Mg[B(hfip)₄]₂/DOX, Mg[B(hfip)₄]₂/DME, and Mg[B(hfip)₄]₂/(DME + DOX), respectively. As illustrated in Figure 7a, the Mg//Cu asymmetric cell with the Mg[B(hfip)₄]₂/DME electrolyte gradually fails after 600 cycles, delivering an average coulomb efficiency of 95.60 %. In contrast, the cycle life can be significantly increased at a current density of 1.0 mAcm⁻² and 0.5 mAhcm⁻² when DOX is employed either as a co-solvent or as the sole solvent. With the screened Mg[B(hfip)₄]₂/DOX electrolyte, the average CE for Mg

plating/stripping reaches 99.54 % even after 5200 cycles. Compared with DME, the cycle life is extended by nearly an order of magnitude, with a cumulative capacity exceeding 2000 mAcm⁻², surpassing previously reported results, as shown in Figure S38 (Supporting Information). Additionally, the performance of cells using the Mg[B(hfip)₄]₂/DOX electrolyte was further evaluated at higher current densities. When the current density and deposition capacity increases to 3.0 mAcm⁻² and 1.0 mAhcm⁻², the Mg anode exhibited reversibly plating/stripping over 2000 cycles, maintaining an average CE of 99.59 %. As shown in Figure 7b, the Mg//Mg symmetric cell demonstrates excellent compatibility between DOX and the Mg metal anode. At a high current density of 2.0 mAcm⁻², the Mg[B(hfip)₄]₂/DOX electrolyte enables stable and reversible Mg plating/stripping for over 3000 cycles, whereas the Mg[B(hfip)₄]₂/DME electrolyte experiences short-circuiting after \approx 735 cycles. Figure S27a (Supporting Information) further illustrates that the Mg//Mg cell with the screened DOX solvent can maintain the stable cycling performance even at an increased current density from 0.5 to 5.0 mAcm⁻². Linear sweep voltammetry (LSV) was also conducted to evaluate the oxidation stability of the Mg[B(hfip)₄]₂/DOX electrolyte, as shown in Figure S36 (Supporting Information). The oxidation voltages of the electrolyte with stainless steel (SS) current collectors exceeds 3.0 V versus Mg/Mg²⁺, demonstrating that the Mg[B(hfip)₄]₂/DOX electrolyte is compatible with a wide range of cathode materials for Mg metal batteries. These experiments not only demonstrate the superior performance of DOX but also confirm the suitability of the Mg[B(hfip)₄]₂/DOX electrolyte for high-voltage Mg battery applications. Additionally, the electrochemical performance of the screened solvent DMP was also evaluated, as illustrated in Figures S41–S43 (Supporting Information), as well as S45. DMP exhibited a relatively high

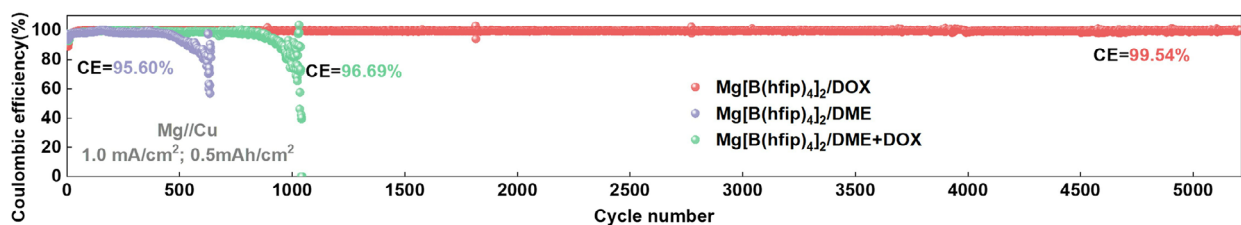
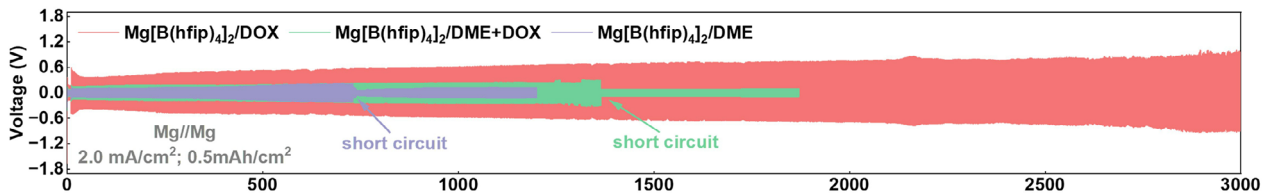
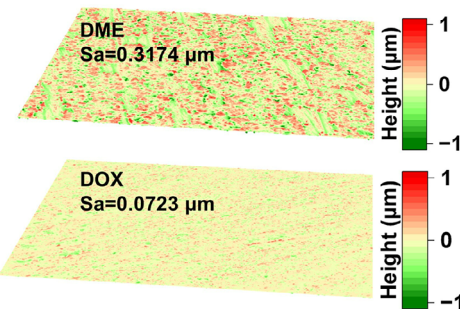
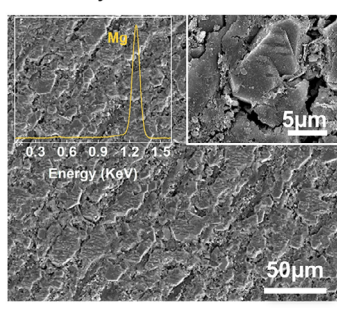
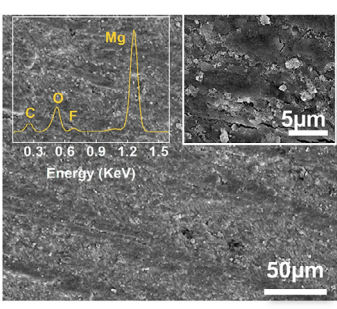
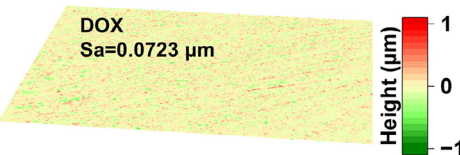
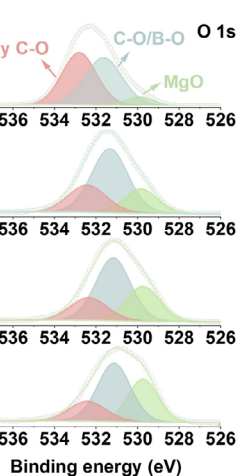
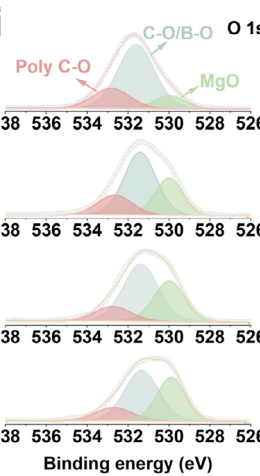
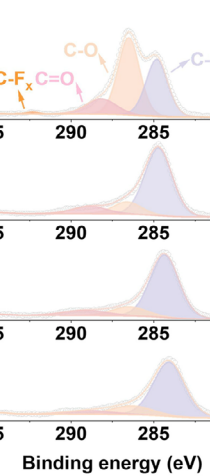
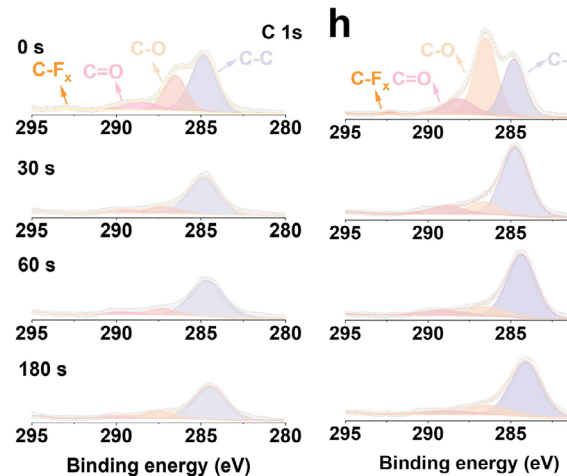
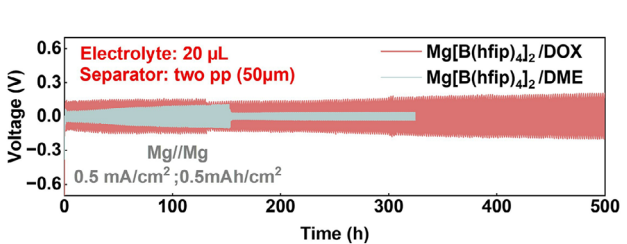
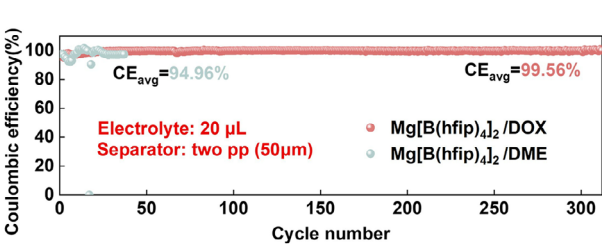
a**b****c****e****f****d****g****k**

Figure 7. a) The CEs of Mg/Cu cells and b) voltage profiles of Mg/Mg cells in the Mg[B(hfip)4]2/DME, Mg[B(hfip)4]2/DOX, and Mg[B(hfip)4]2/(DME + DOX) electrolytes. The CLSM optical images of Mg electrodes cycled in the c) Mg[B(hfip)4]2/DME and d) Mg[B(hfip)4]2/DOX and electrolytes. The SEM images of Mg electrodes after cycling in the e) Mg[B(hfip)4]2/DME and f) Mg[B(hfip)4]2/DOX electrolytes. g–j) C 1s and O 1s XPS spectra with various Ar⁺ sputtering times of Mg electrodes cycled in the (g,i) Mg[B(hfip)4]2/DME and (h,j) Mg[B(hfip)4]2/DOX electrolytes. k) The CEs of Mg/Cu cells and l) voltage profiles of Mg/Mg cells using 20 μL electrolytes and 50 μm separators.

overpotential of 340 mV and a lower CE of 94.19 %. In contrast, the DMP:DME (1:1) co-solvent system demonstrated a reduced overpotential of \approx 270 mV and an improved CE to 95.75 %. Although the observed performance was not particularly outstanding, these results nonetheless confirm acceptable compatibility between the screened solvents and the Mg anode, especially when compared to those obtained through conventional trial-and-error approaches. Moreover, recent reactive molecular dynamics simulations have confirmed that cyclic ether solvents surpass their linear counterparts in enhancing Mg battery stability, thereby offering a mechanism basis for the markedly superior performance of DOX relative to DMP observed in the screening.^[73]

As shown in Figure 7c–j, detailed interfacial characterizations were conducted to elucidate the underlying mechanisms responsible for the impressive electrochemical performance of the Mg[B(hfip)₄]₂/DOX electrolyte. Figure 7c,d depicts that the surface asperity (Sa) of Mg in the Mg[B(hfip)₄]₂/DOX electrolyte was measured at 0.0723 μ m, which is significantly lower than that observed in the Mg[B(hfip)₄]₂/DME electrolyte, i.e., 0.3174 μ m. The corresponding SEM images confirm this observation, revealing that the Mg foil exhibits an uneven surface with prominent cracks after cycling in the Mg[B(hfip)₄]₂/DME electrolyte, as illustrated in Figure 7e. In contrast, Figure 7f shows that the Mg surface appears smooth and dense after cycling in the Mg[B(hfip)₄]₂/DOX electrolyte, with an organic polymer film covering it. Surface EDS analysis was subsequently conducted to further determine the composition of the interfacial film. Where only the Mg element can be observed in the Mg[B(hfip)₄]₂/DME electrolyte, substantial amounts of C and O species are detected in the Mg[B(hfip)₄]₂/DOX system, potentially originating from the decomposition of DOX. The LUMO energy level serves as an indicator of redox stability as mentioned in Section 2.1, thus the corresponding results of these two solvents are presented in Figure S30 (Supporting Information) to validate the proposed hypothesis. The LUMO energy level of DOX is lower than that of DME, i.e., 0.302 and 0.379 eV, indicating that DOX preferentially undergoes a reduction reaction, leading to the SEI formation on the Mg surface. To further investigate the compositional distribution at the Mg anode interface, XPS depth profiling was performed, as illustrated in Figure 7g–j. Compared to the Mg[B(hfip)₄]₂/DME electrolyte, the pronounced signals corresponding to C – O, C = O, and poly C – O species in the Mg[B(hfip)₄]₂/DOX system indicate that DOX undergoes *in situ* decomposition on the Mg surface, leading to the formation of a robust SEI enriched with organic polymer components. Furthermore, the F 1s and B 1s XPS results indicate the presence of anion-derived inorganic species within the SEI, as shown in Figure S39 (Supporting Information). The organic polymer components are expected to provide mechanical flexibility, and the inorganic species enhance Mg²⁺ conductivity. Due to these synergistic effects, the organic-inorganic hybrid SEI significantly enhances the stability of the Mg anode by promoting uniform and stable Mg plating/stripping processes. Consequently, the exceptional cycling stability observed in Mg//Cu cells employing the Mg[B(hfip)₄]₂/DOX electrolyte can be attributed to the *in situ* formation of this robust SEI on the Mg metal surface.

To achieve the satisfactory electrochemical performance, most currently reported Mg metal batteries are evaluated using excessively large electrolyte volume (typically $>100 \mu$ L in a 2032 coin cell) and thick glass fiber separator (e.g., GF/A: 260 μ m, 53 gm^{-3} ; GF/B: 675 μ m, 143 gm^{-3} ; GF/D: 675 μ m, 121 gm^{-3} ; GF/F: 420 μ m, 75 gm^{-3}). However, the use of excessive electrolyte and thick separators inevitably compromises the energy density of Mg batteries. To further demonstrate the advantages of DOX, Mg deposition/dissolution behaviors were investigated under more stringent conditions, specifically with a lean electrolyte and a thin separator. Under more practical conditions, i.e., 20 μ L of electrolyte and two layers of 25 μ m Celgard polypropylene (PP) separators, were employed to assess the application potential of the Mg[B(hfip)₄]₂/DOX electrolyte. As shown in Figure 7k,i, the Mg plating/stripping efficiency in the Mg[B(hfip)₄]₂/DOX electrolyte exhibits remarkable reversibility, sustaining stable operation for over 500 h at 0.5 mAcm⁻² (0.5 mAcm⁻²), and the average CE remains as high as 99.56 % over 300 cycles. Nevertheless, both Mg//Mg and Mg//Cu cells employing the Mg[B(hfip)₄]₂/DME electrolyte experienced rapid short-circuiting. To further verify the practical applicability of the Mg[B(hfip)₄]₂/DOX electrolyte, a soft-packaged Mg//Mg pouch cell was assembled, as shown in Figure S48 (Supporting Information). The experimental conditions were as follows: Mg electrodes with dimensions of 4.0 cm \times 4.0 cm, two layers of 25 μ m-thick Celgard polypropylene separators, and a total electrolyte volume of 320 μ L, i.e., 20 μLcm^{-2} . Under these conditions, the cell maintained continuous and stable cycling for over 300 cycles without short-circuiting, demonstrating the suitability of the electrolyte for practical high-energy-density Mg battery configurations. In addition to Mg[B(hfip)₄]₂, other Mg salts, such as MLCC and Mg(OTf)₂, were also selected to further verify the broader applicability of DOX. As shown in Figure S40a (Supporting Information), the Mg//Cu cell employing the MLCC/(THF + 10 % DOX) electrolyte operates stably at current densities of 2.0 and 4.0 mAcm⁻², achieving a high coulombic efficiency of 99.67 % over 1600 cycles. Figure S40b–e (Supporting Information) further demonstrates the broad applicability of DOX across various Mg salts and solvents, including Mg(TFSI)₂, Mg(OTf)₂, MOPA, MOEA, PrIm, and TEP. It is evident that all corresponding electrolyte systems exhibit satisfactory electrochemical performance, without experiencing rapid short-circuiting. Moreover, as shown in Figures S37–S40 (Supporting Information), the DOX solvent exhibits superior electrochemical performance compared to other solvent systems, even when used as a co-solvent and across various Mg salts.

The applicability of this research paradigm was further assessed and a preliminary test was conducted in discovering new solvents for other battery systems. As an initial attempt, the same database used in this study was also employed in screening solvents for Na and K batteries, i.e., 823 molecules. The constructed molecular database was originally designed for Mg batteries and may not be fully suitable for Na or K battery systems. As shown in Table S16 (Supporting Information), FEC, EC, DEC, diglyme, and DME are selected to define the screening range, and the resulting candidate solvents are illustrated in Figure S46 (Supporting Information). In the absence of predefined

conditions, a total of 12 solvents were successfully identified using this methodology. It is noteworthy that, the screened DEM (CCOCOCC) was recently reported as a co-electrolyte in K batteries,^[74] and DOL (C1COCO1) has also been employed as the primary solvent in Na batteries.^[75] In addition to the reported findings, the screened solvents COC(C)OC and CCOC(C)OCC were selected for experimental validation to further demonstrate the applicability of the proposed methodology. Figure S47 (Supporting Information) presents the corresponding electrochemical performance, demonstrating that the introduction of the screened solvents can enhance the cycling stability of both Na and K battery systems. It should also be acknowledged that the presented results are not comprehensive, and further optimization of certain experimental details is necessary to achieve high-performance batteries. Moreover, these two molecules have not previously been reported for use in either Na or K batteries, thereby demonstrating the effectiveness of this methodology in identifying novel solvents for battery materials. In summary, four of the sixteen screened candidates, including DEM and DOL, have either been previously reported for use in Na-ion/K-ion batteries or experimentally validated in this study, demonstrating extended cycling life and low overpotential. Therefore, despite relying on a relatively small and imperfect molecular database, the methodology achieved a notably high success rate (25 %) in identifying new candidate solvents, i.e., CCOCOCC, C1COCO1, COC(C)OC, and CCOC(C)OCC.

These findings validate the high efficiency of the proposed research paradigm and demonstrate its potential to significantly reduce the cost and effort associated with conventional trial-and-error approaches.^[74–76] Moreover, three solvents (TCEP, 2-CEE, and 2-EtOPyr), previously identified as unsuitable for Mg electrolytes in earlier trial-and-error studies, were used as the counterexamples. As illustrated in Table S17 (Supporting Information), the properties of these solvents are deviated from the defined screening range, indicating they cannot meet the theoretical criteria in Figure 6a. Therefore, it is not surprising that the MLCC electrolyte completely fails after adding a small amount of TCEP/2-CEE/2-EtOPyr, as shown in Figure S44 (Supporting Information), due to their unmatched physicochemical properties. These findings confirm the feasibility of this method for rapidly screening potential organic solvents compatible with Mg anodes from a reverse perspective.

In summary, the aforementioned results demonstrate the applicability of this high-throughput screening research paradigm, which holds substantial promise for advancing the discovery of new solvents for Mg batteries. Moreover, it should also be acknowledged that the interpretability of the proposed screening criteria may not be perfect and could be influenced by human intervention in this study. To address this limitation, efforts are currently underway to employ a graph neural network (GNN) algorithm to more accurately predict physicochemical properties and establish data-driven screening criteria, as illustrated in Figure S4 (Supporting Information). Specifically, the GNN model enhances generalizability and eliminates reliance on pre-defined descriptors by leveraging atom-level features and bonding topology through message passing, thereby predicting molecular properties with improved interpretability. Moreover, by uti-

lizing the GNN model, the predictive performance is significantly improved, as shown in Figures S5 and S6 (Supporting Information), which will be further elaborated in forthcoming work.

3. Conclusion

This study, inspired by the recently emerging generative AI technologies, aims to introduce a top-down reverse research paradigm for screening candidate solvents from a virtual database. Accordingly, a self-developed matrix engineering algorithm has been proposed to generate solvent molecules, enabling precise control over molecular structures and facilitating the selective inclusion or exclusion of specific functional groups. Acids, alcohols, and carbonyl groups which are considered to be unsuitable for Mg batteries are systematically excluded, yielding a more refined virtual molecular library. The generated molecules are classified into four categories, i.e., chain with C = C bonds (644), chain with C – C bonds (106), ring with C = C bonds (56), and ring with C – C bonds (17). The corresponding physicochemical properties are primarily governed by the presence of C – C or C = C bonds, with minimal influence from the structure, such as chain or ring configuration. Specifically, molecules containing C = C bonds generally exhibit the lower LUMO energy levels and the smaller E_g values compared to those with C – C bonds, which range from -2.0 to 0.5 eV and 4.0 to 7.0 eV, respectively. The proportional relationship between E_b and ESP_{\min} suggests that molecules with more electronegative surfaces facilitate stable coordination with Mg^{2+} . Subsequently, a total of 13 ML algorithms are employed to further investigate these physicochemical properties, and LUMO, ΔLUMO , ESP_{\min} , ESP_{\max} , and E_b are selected to establish the screening criteria based on their corresponding MAE results. As anticipated, 18 target solvents are identified through statistical analysis and comparison of their physicochemical properties, narrowing the pool from 823 candidates and improving efficiency nearly 50-fold. DMP and DOX are randomly selected for experimental validation, with DOX significantly improving the electrochemical performance of Mg batteries. At a current density of 1.0 mA cm^{-2} , the average coulombic efficiency for Mg plating/stripping reaches 99.54 % even after 5200 cycles, with a cumulative capacity exceeding 2000 mA cm^{-2} , surpassing previously reported results. Furthermore, additional tests under more stringent conditions, i.e., including the use of a lean electrolyte and a thin separator, are also conducted to further demonstrate the advantages of DOX. Thereafter, three solvents previously identified as unsuitable for Mg batteries through earlier trial-and-error research are re-examined. Computational analysis and battery cycling experiments further validate that solvents failing to meet the established standards can rapidly lead to Mg battery failure. This interesting phenomenon confirms the feasibility of this research paradigm from a reverse perspective. In summary, this work integrates theoretical calculations, ML algorithms, high-throughput screening, and experimental validation, and proposes a new paradigm for the development of solvents for Mg batteries. This study opens new avenues for the future design and optimization of organic solvents and holds the potential to fundamentally transform traditional concepts of solvent design.

4. Experimental Section

Molecular Generation Algorithm: A matrix engineering algorithm was utilized to define node atoms and connecting bonds, thereby enabling the systematic and dynamic construction of molecules, and the schematic illustration is shown in Figure S1 (Supporting Information). Specifically, the matrix size was determined based on the number of atoms required to construct the target molecule. The first row and column of the matrix represented different atom types, with 6 and 8 denoting carbon (C) and oxygen (O) atoms, respectively. For instance, when a molecule contains eight main atoms, e.g., C and O, the matrix size was set to 9 × 9. The connections between various atoms were controlled by the matrix elements, where 1 and 2 represent single and double bonds, respectively, e.g., C – C and C = C. By traversing the upper triangular region of the matrix using a backtracking algorithm, all potential combinations of elements can be thoroughly explored. Following the establishment of atomic and bond configurations, a set of predefined screening criteria is further applied to exclude molecules that fail to meet the specified requirements. In this study, additional filtering has been performed to exclude molecules deemed unsuitable for Mg batteries or containing specific functional groups, such as acids, alcohols, bridgehead carbons, peroxides, and ketones.^[77] The generated molecules were represented in SMILES (Simplified Molecular Input Line Entry System) format,^[78] which includes 823 items and is shown in File S1 (Supporting Information). Python scripts were employed to convert them into 3D structural files and batch-generate input files for subsequent calculations. To demonstrate the applicability of this self-developed algorithm, molecules containing nine main atoms are also generated, yielding a total of 3123 molecular structures, as detailed in File S2 (Supporting Information). Notably, molecules containing modified atoms nitrogen (N), phosphorus (P), fluorine (F), and chlorine (Cl) were also generated to further validate the versatility and effectiveness of this approach, as illustrated in Figures S2 and S3 (Supporting Information). Notably, the concept of molecular generation is employed from an application-oriented perspective, specifically referring to the creation of novel candidate molecules, rather than adhering to the strict algorithmic definition commonly associated with generative models.

Quantum Chemical Calculations: Quantum chemical calculations for the constructed virtual molecular database were conducted via the Gaussian software package,^[79] employing the Lee-Yang-Parr (UB3LYP) functional^[80–82] in conjunction with the 6-311+G(d,p) basis set.^[83–85] Thereafter, frequency calculations were carried out at the same theoretical level and basis set to confirm that the optimized structures corresponded to local energy minima. To account for the solvation effect, the SMD-GIL model was adopted in this study.^[86] All SMD parameters, except for aromaticity and halogenicity, were set to the average values of experimentally determined ionic liquid parameters, facilitating the convenient simulation of physicochemical properties. Based on the optimized molecular structure, the following physicochemical properties were collected: the highest occupied molecular orbital (HOMO) energy level, the lowest unoccupied molecular orbital (LUMO) energy level, the energy gap ($E_g = \text{LUMO} - \text{HOMO}$), the maximum positive surface potential (ESP_{\max}), the minimum negative potential (ESP_{\min}), the binding energy between Mg^{2+} and the solvent (E_b), and the change in LUMO energy level upon Mg^{2+} coordination ($\Delta\text{LUMO} = \text{LUMO}_{\text{Mg}} - \text{LUMO}$).

Machine Learning Methods: All machine learning (ML) algorithms were implemented via the open-source code Scikit-learn package within the Python3 environment.^[87] 13 different ML algorithms were selected for model training and performance evaluation, including Support Vector Regression (SVR), Random Forest (RF), Gradient Boosting Regression (GBR), Linear Regression (LR), Decision Tree (DT), K-Nearest Neighbors (KNN), Bayesian Regression (BR), Extreme Gradient Boosting Regression (XGBR), Ridge Regression (Ridge), Extra Trees Regression (ETR), Kernel Ridge Regression (KRR), Bagging, and Artificial Neural Networks (ANN). The dataset for ML consisted of 823 solvent molecules, each annotated with the above-mentioned physicochemical properties. The following molecular characteristics were employed as features, including molecular radius (R), average ionization energy (AvgI), average electronegativity (AvgX), average electron affinity (AvgE), dipole moment (μ), degree of un-

saturation (DoU), molecular mass (Mr), Mulliken charge of Mg^{2+} (Mc), Mg – O bond length (BL), number of oxygen atoms (NumO), number of carbon atoms (NumC), number of hydrogen atoms (NumH), carbon–oxygen ratio (rCO), and total number of main atoms (NumA).^[88]

$$\text{AvgI} = \frac{xI_C + yI_H + zI_O}{x + y + z} \quad (1)$$

$$\text{AvgX} = \frac{xX_C + yX_H + zX_O}{x + y + z} \quad (2)$$

$$\text{AvgE} = \frac{xE_C + yE_H + zE_O}{x + y + z} \quad (3)$$

$$\text{DoU} = \frac{2n(C) + 2 - n(H)}{2} \quad (4)$$

where x , y , z represent the number of C, H and O atoms, respectively. I , X , and E can be obtained from the periodic table, and the parameter names along with their corresponding abbreviations are provided in Table S1 (Supporting Information).

To assess the generalization capability of ML models on unseen data, the dataset was partitioned into training and test sets with an 80:20 ratio. Hyperparameter optimization was conducted using grid search to identify the parameter configuration that maximized the model performance. Given the limited size of the dataset, i.e., 823 molecules, the training set was not further divided to include a separate validation set. Instead, model training and hyperparameter tuning, e.g., grid search, were performed directly on the training data. Notably, the evaluation was conducted on a held-out 20% test set, in accordance with standard practices for small-sample machine learning. The coefficient of determination (R^2) and the mean absolute error (MAE) were employed as evaluation metrics to assess overall model efficacy, as presented below.

$$R^2 = \frac{\sum(x_i - \bar{x})(y_i - \bar{y})}{\sum(x_i - \bar{x})^2} \quad (5)$$

$$\text{MAE} = \frac{1}{n} \sum_{i=1}^n |\hat{y}_i - y_i| \quad (6)$$

$$p = \frac{\sum_i(x - \mu_x)(y - \mu_y)}{\sqrt{\sum_i(x - \mu_x)^2 \sum_i(y - \mu_y)^2}} \quad (7)$$

In addition, the Pearson correlation coefficient was utilized to quantify the correlations between features, as defined by Equation (7). The coefficient ranges from -1 to 1 , indicating both the strength and direction of the relationship between x and y variables, where positive values signify a positive correlation and vice versa.^[89] The absolute of coefficient values greater than 0.8 indicate a strong correlation, less than 0.5 denotes a weak correlation, and between 0.5 and 0.8 signify a moderate correlation.

Materials and Preparation: To validate the effectiveness of the screened solvents for Mg metal batteries, electrochemical cells were fabricated and their corresponding performance was systematically evaluated.

Materials and Preparation—Materials: Anhydrous magnesium chloride (MgCl_2 , 99.99%) and lithium chloride (LiCl , 99.995 %) were obtained from Alpha Pharmaceutical Co., Ltd. and used without further purification. Anhydrous tetrahydrofuran (THF, 99%), 1,2-Dimethoxyethane (DME, 99%) were purchased from Suzhou Duoduo Chem Co., Ltd. Magnesium Bis(trifluoromethanesulfonyl)imide ($\text{Mg}(\text{TFSI})_2$, 97%) and Magnesium trifluoromethanesulfonate ($\text{Mg}(\text{OTf})_2$, 98 %) were purchased from Aladdin and dried at 100 °C for at least 48 h to remove residual moisture. Hexafluoroisopropanol (HFIP, 99 %), 1.0 M $\text{Zn}(\text{BH}_4)_2$ /THF, 1,3-Dioxane (DOX, 98 %), 1,2-Dimethoxypropane (DMP, 98 %), 1,1,2-Trimethoxyethane (TME, 98 %), 2-Methoxyethylamine (MOEA, 98 %), 3-Methoxypropylamine (MOPA, 99 %), 1-Propylimidazole (PrIm, 98 %), 1,2-Bis(2-chloroethoxy)ethane (2-CEE, 98 %), Tris(2-chloroethyl) phosphate

(TCEP, 98 %), and 2-Ethoxypyrazine (2-EtOPyr, 98 %) were purchased from Aladdin and dried with molecular sieves prior to use. All synthesis experiments were conducted in an argon-filled glovebox with water and oxygen concentrations below 0.1 ppm.

Materials and Preparation—Electrolyte Preparation: The Mg[B(hfip)₄]₂-based electrolyte was synthesized following a previously reported method.^[26] Specifically, 2 mL Zn(BH₄)₂/THF solution was dissolved into 2 mL DME in a glass bottle, and a mixture of hexafluoroisopropanol (2.689 g) and DME (1 mL) was then gradually added under continuous stirring. The resulting solution was stirred for over 24 h, after which Mg foils were immersed in the solution without stirring until the surface was free of any black Zn deposits. After filtration and vacuum drying at 60 °C, the Mg[B(hfip)₄]₂ salt was obtained. Then, 0.829 g of Mg[B(hfip)₄]₂ salt was added to 2 mL of DME or DOX and stirred for 12 h to prepare the Mg[B(hfip)₄]₂/DME or Mg[B(hfip)₄]₂/DOX electrolyte, each with a concentration of 0.3 M. For the preparation of the magnesium–lithium chloride complex (MLCC) electrolyte, 0.3 M MgCl₂ (114.25 mg) and 0.3 M LiCl (50.85 mg) were dissolved in 4 mL of THF and stirred for 24 h to obtain the MLCC/THF electrolyte. The MLCC/THF+10 % DOX or MLCC/THF+10 % DMP electrolytes were prepared by adding 10 % vol DOX or DMP into the MLCC/THF solution. The Mg[B(hfip)₄]₂⁻, Mg(TFSI)₂⁻, and Mg(OTf)₂⁻ based electrolytes were obtained by mixing the corresponding Mg salts and the appropriate solvents at room temperature for 24 h to yield clear solutions. In all cases, the concentration of Mg²⁺ was maintained at 0.3 M.

Materials and Preparation—Electrochemical Measurements: The 2032 coin cells were assembled in an argon-filled glovebox, with H₂O and O₂ levels maintained below 0.1 ppm. Each cell comprised polished Mg foils (Φ12 mm, 100 µm), Whatman glass fibers (GF/B, Φ19 mm) separators, and 120 µL of electrolyte. For the lean electrolyte test, 20 mL of electrolyte was used in combination with two layers of 25 µm Celgard 2500 polypropylene (PP) separators. The Mg//Cu and Mg//Mg cells were assembled to evaluate coulombic efficiency (CE), polarization voltage, and long-term cycling performance of electrolytes formulated with the newly developed solvents.

Materials and Preparation—Materials Characterizations: Surface morphology and roughness were analyzed using a confocal laser scanning microscope (CLSM, Sensofar S.L.). Scanning electron microscopy (SEM) and energy-dispersive spectrometry (EDS) were conducted using a field emission scanning electron microscope (Nova NanoSEM 230). After electrochemical cycling, the Mg metal electrodes were extracted from the cells, rinsed with DME, and dried inside an argon-filled glove box. The cycled Mg metal electrodes were then characterized by SEM and X-ray photoelectron spectroscopy (XPS, Thermo Fisher). To prevent adhesion of the electrode to the glass fiber during the plating/stripping process, a layer of Celgard 2500 was placed between the glass fiber separator and the Mg electrode.

Supporting Information

Supporting Information is available from the Wiley Online Library or from the author.

Acknowledgements

X.G. and A.-Q.Y. contributed equally to this work. This work was supported by the National Natural Science Foundation of China (No. 52503286 and No. 22409030), the Natural Science Foundation of Fujian Province, China (No. 2024J01259 and No. 2024J08028), the Pilot Group Program of the Research Fund for International Senior Scientists (No. 22250710676), and the National Key R&D Program of China (No. 2022YFB4004100). The authors also acknowledged the Foundation from Hubei University of Technology (No. 202307A08).

Conflict of Interest

The authors declare no conflict of interest.

Data Availability Statement

Data available on request from the authors

Keywords

dox, generative artificial intelligence, mg metal batteries, solvent screening, virtual molecular database

Received: May 28, 2025
Revised: September 4, 2025
Published online:

- [1] J. Zhu, Y. Wang, Y. Huang, R. Bhushan Gopaluni, Y. Cao, M. Heere, M. J. Mühlbauer, L. Mereacre, H. Dai, X. Liu, A. Senyshyn, X. Wei, M. Knapp, H. Ehrenberg, *Nat. Commun.* **2022**, *13*, 2261.
- [2] C.-Y. Wang, T. Liu, X.-G. Yang, S. Ge, N. V. Stanley, E. S. Rountree, Y. Leng, B. D. McCarthy, *Nature* **2022**, *611*, 485.
- [3] J. Xu, J. Zhang, T. P. Pollard, Q. Li, S. Tan, S. Hou, H. Wan, F. Chen, H. He, E. Hu, Kang Xu, X.-Q. Yang, O. Borodin, C. Wang, *Nature* **2023**, *614*, 694.
- [4] S. Zhang, J. Ma, S. Dong, G. Cui, *Electrochim. Energy Rev.* **2023**, *6*, 4.
- [5] Z. Tang, S. Zhou, Y. Huang, H. Wang, R. Zhang, Q. Wang, D. Sun, Y. Tang, H. Wang, *Electrochim. Energy Rev.* **2023**, *6*, 8.
- [6] X. Chen, W. Li, D. Reed, X. Li, X. Liu, *Electrochim. Energy Rev.* **2023**, *6*, 33.
- [7] T. Bashir, S. Zhou, S. Yang, S. A. Ismail, T. Ali, H. Wang, J. Zhao, L. Gao, *Electrochim. Energy Rev.* **2023**, *6*, 5.
- [8] M. Li, J. Lu, Z. Chen, K. Amine, *Adv. Mater.* **2018**, *30*, 1800561.
- [9] A. Manthiram, *Nat. Commun.* **2020**, *11*, 1550.
- [10] F. Duffner, N. Kronemeyer, J. Tübke, J. Leker, M. Winter, R. Schmuck, *Nat. Energy* **2021**, *6*, 123.
- [11] H. Dong, O. Tutusaus, Y. Liang, Y. Zhang, Z. Lebens-Higgins, W. Yang, R. Mohtadi, Y. Yao, *Nat. Energy* **2020**, *5*, 1043.
- [12] C. Li, R. D. Guha, A. Shyamsunder, K. A. Persson, L. F. Nazar, *Energy Environ. Sci.* **2024**, *17*, 190.
- [13] M. Li, R. P. Hicks, Z. Chen, C. Luo, J. Guo, C. Wang, Y. Xu, *Chem. Rev.* **2023**, *123*, 1712.
- [14] Y. Liang, Y. Yao, *Nat. Rev. Mater.* **2023**, *8*, 109.
- [15] P. Canepa, G. Sai Gautam, D. C. Hannah, R. Malik, M. Liu, K. G. Gallagher, K. A. Persson, G. Ceder, *Chem. Rev.* **2017**, *117*, 4287.
- [16] H. Zhang, L. Qiao, M. Armand, *Angew. Chem. Int. Ed.* **2022**, *61*, 202214054.
- [17] Y. S. Meng, V. Srinivasan, K. Xu, *Science* **2022**, *378*, eabq3750.
- [18] J. B. Goodenough, Y. Kim, *Chem. Mater.* **2010**, *22*, 587.
- [19] J. B. Goodenough, K.-S. Park, *J. Am. Chem. Soc.* **2013**, *135*, 1167.
- [20] J. Xiao, X. Zhang, H. Fan, Y. Zhao, Y. Su, H. Liu, X. Li, Y. Su, H. Yuan, T. Pan, Q. Lin, L. Pan, Y. Zhang, *Adv. Mater.* **2022**, *34*, 2203783.
- [21] J. Long, S. Tan, J. Wang, F. Xiong, L. Cui, Q. An, L. Mai, *Angew. Chem., Int. Ed.* **2023**, *62*, 202301934.
- [22] K. A. See, K. W. Chapman, L. Zhu, K. M. Wiaderek, O. J. Borkiewicz, C. J. Barile, P. J. Chupas, A. A. Gewirth, *J. Am. Chem. Soc.* **2016**, *138*, 328.
- [23] H. S. Kim, T. S. Arthur, G. D. Allred, J. Zajicek, J. G. Newman, A. E. Rodnyansky, A. G. Oliver, W. C. Boggess, J. Muldoon, *Nat. Commun.* **2011**, *2*, 427.
- [24] S. Hou, X. Ji, K. Gaskell, P.-f. Wang, L. Wang, J. Xu, R. Sun, O. Borodin, C. Wang, *Science* **2021**, *374*, 172.
- [25] D. Zhang, Y. Wang, Y. Yang, Y. Zhang, Y. Zhao, M. Pan, Y. Sun, S. Chen, X. Liu, J. Wang, Y. NuLi, *Adv. Energy Mater.* **2023**, *13*, 2301795.
- [26] S. Li, J. Zhang, S. Zhang, Q. Liu, H. Cheng, L. Fan, W. Zhang, X. Wang, Q. Wu, Y. Lu, *Nat. Energy* **2024**, *9*, 285.

- [27] E. N. Keyzer, J. Lee, Z. Liu, A. D. Bond, D. S. Wright, C. P. Grey, *J. Mater. Chem. A* **2019**, *7*, 2677.
- [28] D. Aurbach, Z. Lu, A. Schechter, Y. Gofer, H. Gizbar, R. Turgeman, Y. Cohen, M. Moshkovich, E. Levi, *Nature* **2000**, *407*, 724.
- [29] Z. Zhao-Karger, X. Zhao, D. Wang, T. Diemant, R. J. Behm, M. Fichtner, *Adv. Energy Mater.* **2015**, *5*, 1401155.
- [30] A. Yang, X. Gao, M. Pei, J. Zhou, H. Wang, C. Liao, W. Yan, J. Xiao, Y. Liu, J. Zhang, *Angew. Chem.* **2025**, *137*, 202424237.
- [31] Y. Deng, G. Li, R. Deng, B. Zhang, L. Cao, G. Huang, J. Wang, F. Pan, *Angew. Chem.* **2025**, *202513213*.
- [32] T. Lombardo, M. Duquesnoy, H. El-Bouysidy, F. Årén, A. Gallo-Bueno, P. B. Jørgensen, A. Bhowmik, A. Demortière, E. Ayerbe, F. Alcaide, M. Reynaud, J. Carrasco, A. Grimaud, C. Zhang, T. Vegge, P. Johansson, A. A. Franco, *Chem. Rev.* **2021**, *122*, 10899.
- [33] A. Walsh, *Nat. Chem.* **2015**, *7*, 274.
- [34] N. H. Park, M. Manica, J. Born, J. L. Hedrick, T. Erdmann, D. Y. Zubarev, N. Adell-Mill, P. L. Arrechea, *Nat. Commun.* **2023**, *14*, 3686.
- [35] Q. Zhang, Y. Hu, J. Yan, H. Zhang, X. Xie, J. Zhu, H. Li, X. Niu, L. Li, Y. Sun, W. Hu, *Adv. Mater.* **2024**, *36*, 2405163.
- [36] C. Zhu, E. A. Bamidele, X. Shen, G. Zhu, B. Li, *Chem. Rev.* **2024**, *124*, 4258.
- [37] N. Yao, X. Chen, Z.-H. Fu, Q. Zhang, *Chem. Rev.* **2022**, *122*, 10970.
- [38] M. Abolhasani, E. Kumacheva, *Nat. Synth.* **2023**, *2*, 483.
- [39] J. Wu, L. Torresi, M. Hu, P. Reiser, J. Zhang, J. S. Rocha-Ortiz, L. Wang, Z. Xie, K. Zhang, B.-w. Park, et al., *Science* **2024**, *386*, 1256.
- [40] Q. Jia, H. Liu, X. Wang, Q. Tao, L. Zheng, J. Li, W. Wang, Z. Liu, X. Gu, T. Shen, S. Hou, Z. Jin, J. Ma, *Angew. Chem., Int. Ed.* **2025**, *64*, 202424493.
- [41] G. Xu, Y. Li, J. Li, J. Li, X. Liu, C. Wang, W. Mai, G. Yang, L. Pan, *Angew. Chem.* **2025**, *202511389*.
- [42] R. Li, W. Zhao, Z. Fan, M. Zhang, J. Li, R. Li, Z. Zuo, X. Yang, *Energy Environ. Sci.* **2025**, *18*, 6790.
- [43] S. Han, Y. Zheng, X. Zhang, S. Alshammari, W. Fan, S. Yin, Z. M. El-Bahy, H. K. Thabet, S. Gong, B. Lu, Y. Liu, J. Zhou, *Adv. Mater.* **2025**, *11814*.
- [44] S. Eswarappa Prameela, T. M. Pollock, D. Raabe, M. A. Meyers, A. Aitkaliyeva, K.-L. Chintersingh, Z. C. Cordero, L. Graham-Brady, *Nat. Rev. Mater.* **2023**, *8*, 81.
- [45] Q. Meng, Y. Huang, L. Li, F. Wu, R. Chen, *Joule* **2024**, *8*, 344.
- [46] P. Zhong, B. Deng, T. He, Z. Lun, G. Ceder, *Joule* **2024**, *8*, 1837.
- [47] Y. Wu, Q. Hu, H. Liang, A. Wang, H. Xu, L. Wang, X. He, *Adv. Energy Mater.* **2023**, *13*, 2300259.
- [48] J. S. Murray, P. Politzer, *Wiley Interdiscip. Rev.: Comput. Mol. Sci.* **2017**, *7*, e1326.
- [49] P. Politzer, J. S. Murray, *Theor. Chem. Acc.* **2002**, *108*, 134.
- [50] J. S. Murray, P. Politzer, *Wiley Interdiscip. Rev.: Comput. Mol. Sci.* **2011**, *1*, 153.
- [51] Y.-C. Gao, N. Yao, X. Chen, L. Yu, R. Zhang, Q. Zhang, *J. Am. Chem. Soc.* **2023**, *145*, 23764.
- [52] Q. Wu, M. T. McDowell, Y. Qi, *J. Am. Chem. Soc.* **2023**, *145*, 2473.
- [53] J. Xiao, X. Zhang, H. Fan, Q. Lin, L. Pan, H. Liu, Y. Su, X. Li, Y. Su, S. Ren, et al., *Adv. Energy Mater.* **2022**, *12*, 2202602.
- [54] C. S. Rustomji, Y. Yang, T. K. Kim, J. Mac, Y. J. Kim, E. Caldwell, H. Chung, Y. S. Meng, *Science* **2017**, *356*, 6345, eaal4263.
- [55] Z. Yu, H. Wang, X. Kong, W. Huang, Y. Tsao, D. G. Mackanic, K. Wang, X. Wang, W. Huang, S. Choudhury, Y. Zheng, C. V. Amanchukwu, S. T. Hung, Y. Ma, E. G. Lomeli, J. Qin, Y. Cui, Z. Bao, *Nat. Energy* **2020**, *5*, 526.
- [56] X. Chen, H.-R. Li, X. Shen, Q. Zhang, *Angew. Chem. Int. Ed.* **2018**, *57*, 16643.
- [57] X. Chen, X. Shen, B. Li, H.-J. Peng, X.-B. Cheng, B.-Q. Li, X.-Q. Zhang, J.-Q. Huang, Q. Zhang, *Angew. Chem. Int. Ed.* **2018**, *57*, 734.
- [58] H. Cheng, Z. Ma, P. Kumar, H. Liang, Z. Cao, H. Xie, L. Cavallo, H. Kim, Q. Li, Y.-K. Sun, J. Ming, *Adv. Energy Mater.* **2024**, *14*, 2304321.
- [59] A. Roy, M. Sotoudeh, S. Dinda, Y. Tang, C. Kübel, A. Groß, Z. Zhao-Karger, M. Fichtner, Z. Li, *Nat. Commun.* **2024**, *15*, 492.
- [60] Y. Wang, N. Wagner, J. M. Rondinelli, *MRS Commun.* **2019**, *9*, 793.
- [61] B. Weng, Z. Song, R. Zhu, Q. Yan, Q. Sun, C. G. Grice, Y. Yan, W.-J. Yin, *Nat. Commun.* **2020**, *11*, 3513.
- [62] J. Schmidt, M. R. Marques, S. Botti, M. A. Marques, *Npj Comput. Mater.* **2019**, *5*, 83.
- [63] T. Gao, X. Ji, S. Hou, X. Fan, X. Li, C. Yang, F. Han, F. Wang, J. Jiang, K. Xu, C. Wang, *Adv. Mater.* **2018**, *30*, 1704313.
- [64] R. Mohtadi, O. Tutusaus, T. S. Arthur, Z. Zhao-Karger, M. Fichtner, *Joule* **2021**, *5*, 581.
- [65] E. Sahadeo, Y. Wang, C.-F. Lin, Y. Li, G. Rubloff, S. B. Lee, *Chem. Comm.* **2020**, *56*, 4583.
- [66] W. Zhang, S. Zhang, L. Fan, L. Gao, X. Kong, S. Li, J. Li, X. Hong, Y. Lu, *ACS Energy Lett.* **2019**, *4*, 644.
- [67] Y.-X. Yao, X. Chen, C. Yan, X.-Q. Zhang, W.-L. Cai, J.-Q. Huang, Q. Zhang, *Angew. Chem. Int. Ed.* **2021**, *60*, 4090.
- [68] K. Kim, J. Kim, J. H. Moon, *Adv. Sci.* **2023**, *10*, 2206057.
- [69] E. Park, J. Park, K. Lee, Y. Zhao, T. Zhou, G. Park, M.-G. Jeong, M. Choi, D.-J. Yoo, H.-G. Jung, A. Coskun, J. W. Choi, *ACS Energy Lett.* **2022**, *8*, 179.
- [70] Y. Liu, H. Zou, Z. Huang, Q. Wen, J. Lai, Y. Zhang, J. Li, K. Ding, J. Wang, Y.-Q. Lan, et al., *Energy Environ. Sci.* **2023**, *16*, 6110.
- [71] J. Bae, H. Park, X. Guo, X. Zhang, J. H. Warner, G. Yu, *Energy Environ. Sci.* **2021**, *14*, 4391.
- [72] S.-B. Son, T. Gao, S. P. Harvey, K. X. Steirer, A. Stokes, A. Norman, C. Wang, A. Cresce, K. Xu, C. Ban, *Nat. Chem.* **2018**, *10*, 532.
- [73] C. Gao, W. Zhao, Y. Gong, Y. Chen, L. Cai, X. Yang, M. Yang, *Energy Storage Mater.* **2025**, *80*, 104361.
- [74] W. Chen, D. Zhang, H. Fu, J. Li, X. Yu, J. Zhou, B. Lu, *ACS nano* **2024**, *18*, 12512.
- [75] C. Wang, A. C. Thenuwara, J. Luo, P. P. Shetty, M. T. McDowell, H. Zhu, S. Posada-Pérez, H. Xiong, G. Hautier, W. Li, *Nat. Commun.* **2022**, *13*, 4934.
- [76] J. Ma, X. Feng, Y. Wu, Y. Wang, P. Liu, K. Shang, H. Jiang, X. Hou, D. Mitlin, H. Xiang, *J. Energy Chem.* **2023**, *77*, 290.
- [77] M. Grünebaum, A. Buchheit, C. Lürenbaum, M. Winter, H.-D. Wiemhöfer, *J. Phys. Chem. C* **2019**, *123*, 7033.
- [78] D. Weininger, *J. Chem. Inf. Comput.* **1988**, *28*, 31.
- [79] M. J. Frisch, G. W. Trucks, H. B. Schlegel, G. E. Scuseria, M. A. Robb, J. R. Cheeseman, G. Scalmani, V. Barone, G. A. Petersson, H. Nakatsuji, X. Li, M. Caricato, A. V. Marenich, J. Bloino, B. G. Janesko, R. Gomperts, B. Mennucci, H. P. Hratchian, J. V. Ortiz, A. F. Izmaylov, J. L. Sonnenberg, D. Williams-Young, F. Ding, F. Lipparini, F. Egidi, J. Goings, B. Peng, A. Petrone, T. Henderson, D. Ranasinghe, et al., Gaussian 16 revision a.03, **2016**, Gaussian Inc., Wallingford, CT.
- [80] A. D. Becke, *J. Chem. Phys.* **1992**, *96*, 2155.
- [81] A. D. Becke, *J. Chem. Phys.* **1992**, *97*, 9173.
- [82] W. Kohn, A. D. Becke, R. G. Parr, *J. Chem. Phys.* **1996**, *100*, 12974.
- [83] R. Krishnan, J. S. Binkley, R. Seeger, J. A. Pople, *J. Chem. Phys.* **1980**, *72*, 650.
- [84] M. J. Frisch, J. A. Pople, J. S. Binkley, *J. Chem. Phys.* **1984**, *80*, 3265.
- [85] P. C. Hariharan, J. A. Pople, *Theor. Chim. Acta* **1973**, *28*, 213.
- [86] V. S. Bernales, A. V. Marenich, R. Contreras, C. J. Cramer, D. G. Truhlar, *J. Phys. Chem. B* **2012**, *116*, 9122.
- [87] F. Pedregosa, G. Varoquaux, A. Gramfort, V. Michel, B. Thirion, O. Grisel, M. Blondel, P. Prettenhofer, R. Weiss, V. Dubourg, et al., *J. Mach. Learn. Res.* **2011**, *12*, 2825.
- [88] T. Lu, F. Chen, *J. Comput. Chem.* **2012**, *33*, 580.
- [89] A. Ly, M. Marsman, E.-J. Wagelmakers, *Stat. Neerl.* **2018**, *72*, 4.